The Astrophysical Journal, 935:37 (23pp), 2022 August 10 https://doi.org/10.3847/1538-4357/ac7b30


# Accreted or Not Accreted? The Fraction of Accreted Mass in Galaxies from the Magneticum Simulations and Observations

Rhea-Silvia Remus[1] and Duncan A. Forbes[2]
[1] Universitäts-Sternwarte München, Fakultät für Physik, LMU München, Scheinerstr. 1, D-81679 München, Germany; rhea@usm.lmu.de
[2] Centre for Astrophysics and Supercomputing, Swinburne University of Technology, Hawthorn VIC 3122, Australia
*Received 2021 November 1; revised 2022 June 8; accepted 2022 June 20; published 2022 August 10*

## Abstract

In the two-phase scenario of galaxy formation, a galaxy's stellar mass growth is first dominated by in-situ star formation, and subsequently by accretion. We analyze the radial distribution of the accreted stellar mass in ∼500 galaxies from the $(48\ \mathrm{Mpc}/h)^3$ box volume of the hydrodynamical cosmological simulation Magneticum, in a stellar-mass range of $10^{10}$ to $10^{12}\ M_\odot$. We find that higher-mass galaxies have larger accreted fractions, as found in previous works, but predict generally higher accretion fractions for low-mass galaxies. Based on the 3D radial distribution of the accreted and in-situ components, we define six galaxy classes, from completely accretion to completely in-situ dominated, and measure the transition radii between in-situ and accretion-dominated regions for galaxies that reveal a transition. About 70% of our galaxies have one transition radius. However, about 10% of the galaxies are accretion dominated everywhere, and about 13% have two transition radii, with the center and the outskirts both being accretion dominated. We show that these classes are strongly correlated with the galaxy merger histories, especially with the cold gas fraction at the time of merging. We find high total in-situ (low accretion) fractions to be associated with smaller, lower-mass galaxies, lower central dark-matter fractions, and larger transition radii. Finally, we show that the dips in observed surface brightness profiles seen in many early-type galaxies do not correspond to the transition from in-situ to accretion-dominated regions, and that any inferred mass fractions are not indicative of the true accreted mass but contain information about the galaxies' dry-merger history.

*Unified Astronomy Thesaurus concepts:* Galaxy structure (622); Galaxy formation (595); Galaxy accretion (575); Galaxy evolution (594)

## 1. Introduction

In the two-phase scenario of galaxy formation (e.g., Oser et al. 2010), galaxies undergo two main phases of growth: first the in-situ and subsequently the ex-situ (or accretion) growth phase. In the former phase, stars are formed within the primary galaxy. In the latter phase, mass growth occurs primarily through the accretion of satellite galaxies. A pioneering work in this area was presented by Oser et al. (2010), using a set of zoom simulations of massive galaxies, who found that the in-situ phase occurs between redshifts 6 and 2, giving rise to a "galaxy core" of size ∼2 kpc, followed by the accretion-dominated growth at lower redshifts. They also find higher-mass galaxies to have higher fractions of accreted mass, and that the accreted mass is more often deposited in galaxy outer halo regions. This has been subsequently supported by parameter studies using binary merger simulations of different mass ratios, demonstrating that larger mass ratios for host and satellite galaxies are more likely to lead to deposition of the accreted stellar mass at larger radii, while small merger mass ratios usually lead to a full mixture of the accreted and in-situ formed stars (e.g., Hilz et al. 2012; Karademir et al. 2019). However, the picture is not that clear, as the orbital configurations of the mergers have been shown to influence the radius of mass deposition for satellite galaxies, especially for mergers of larger mass ratios, with circular orbits leading to mass depositions at larger radii than radial merger orbits (e.g., Amorisco 2017; Karademir et al. 2019).

This two-phase scenario has been further refined over the last decade with increasingly sophisticated, full cosmological simulations. Those focusing on predictions for the accreted stellar component of early-type galaxies (ETGs) include the dark-matter particle tagging approach of Cooper et al. (2013, 2015) and, more recently, hydrodynamical cosmological simulations like Illustris (Pillepich et al. 2014; Rodriguez-Gomez et al. 2016), EAGLE (Qu et al. 2017; Clauwens et al. 2018; Davison et al. 2020), IllustrisTNG (Pillepich et al. 2018; Tacchella et al. 2019; Pulsoni et al. 2021), and in the present work about Magneticum.

In particular, Cooper et al. (2013) modeled 1872 central galaxies in the mass range $10.7 < \log M_* < 11.4$ (i.e., $11.5 < \log M_{200} < 14.0$) using a semianalytic method to tag dark-matter particles, not including a full treatment of gas physics in the simulation itself. Being mainly massive galaxies, the sample is dominated by ETGs. They found that accretion leads to a break, or change, in the slope of the stellar mass surface density profile at the radius where the accreted material starts to dominate over that formed in situ. They fit Sérsic profiles to the in-situ and accreted stars separately in surface density space, finding that the resulting double Sérsic profiles provided a good overall fit. They showed that the fraction of accreted material approaches 100% for the most massive ETGs, with more accretion-dominated galaxies having shallower density profiles with little or no obvious transition in the overall profile. This study was further expanded for the very high-mass end ($\log M_{200} \sim 14$) by Cooper et al. (2015). They found double Sérsic profiles to be a good fit to the stellar mass

surface density profiles, with the inner component having Sérsic indices of $n \sim 4$ and the outer component having $n \sim 1$ (similar to observational results for brightest cluster galaxies (BCGs), e.g., Seigar et al. 2007; Kluge et al. 2020). However, these inner and outer components were found to correspond to the relaxed and unrelaxed accreted stars rather than the in-situ and accreted stars.

Results from the fully hydrodynamical cosmological simulations all confirm the idea of the two-phase scenario of galaxy formation, and the general trend for higher-mass galaxies to have larger amounts of accreted stars and shallower radial stellar density profiles (Pillepich et al. 2014; Rodriguez-Gomez et al. 2016; Tacchella et al. 2019; Davison et al. 2020). They also generally agree that the transition radius between accretion-dominated and in-situ-dominated stars is generally smaller for more massive galaxies. However, they show very different results regarding the details of the accreted versus in-situ components of galaxies, caused by the different subgrid models describing the star formation and feedback processes (see Vogelsberger et al. 2020, for a recent review).

For example, Rodriguez-Gomez et al. (2016) find for the old Illustris simulations that all galaxies reveal a clear "transition" radius for which the in-situ and accreted components contribute equally (i.e., 50:50), while Tacchella et al. (2019) reported for the new IllustrisTNG simulations that their most massive galaxies can be dominated by accreted stars at all radii. In addition, Tacchella et al. (2019) find much higher accreted mass fractions at a given stellar mass for the new IllustrisTNG simulations than Rodriguez-Gomez et al. (2016) found for the old Illustris simulations. Using the EAGLE simulation, Davison et al. (2020) found similar ex-situ fractions as a function of stellar mass as Tacchella et al. (2019). They also confirmed previous findings that the majority of accreted material is deposited in the outer regions, while for the most massive galaxies the accreted mass can dominate over in-situ material in the inner regions. However, the mass–size relations found for the galaxies from these two simulations are different, clearly showing that the details of galaxy formation still strongly differ between the different simulations.[3]

More recently, these studies were also broadened to study the radial kinematic profiles of galaxies as possible tracers for the transition radii from in-situ to accretion-dominated parts of galaxies (e.g., Schulze et al. 2020 using the Magneticum simulations, and Pulsoni et al. 2021 using the IllustrisTNG simulations). Both studies find that the shape of the kinematic profile (i.e., $v/\sigma$ as a function of $r$) does not, in general, trace the transition between in-situ and ex-situ-dominated galaxy regions. Schulze et al. (2020) showed that the kinematic profiles can be used as a tracer for the transition radius only for a special subset of galaxies that only experienced very small mergers since $z \sim 1$; Pulsoni et al. (2021) split their galaxies into four classes of stellar mass density profiles based on the variation of the in-situ and ex-situ fractions with radius. We comment further on their findings in the main sections of this work.

Observationally, the in-situ and accreted components of galaxies are much harder to tackle. Deep imaging studies of massive ETGs found that around 3/4 of their galaxies reveal evidence for substructures in their stellar halos (e.g., Schweizer & Seitzer 1992; Forbes & Thomson 1992; Tal et al. 2009; Duc et al. 2015; Kluge et al. 2020). Such substructures, in the form of shells, plumes, envelopes, etc., likely represent the debris of accreted satellite galaxies. After stacking a large sample of 42,000 luminous red galaxies (with $\log M_* > 11$), Tal & van Dokkum (2011) found that within about 8 $R_e$ their surface brightness profiles could be well represented by a single Sérisc profile, but beyond that, an extra component was required. A transition at similar radii has been reported in the globular cluster systems of massive ETGs (e.g., Forbes & Remus 2018). D'Souza et al. (2014) fit 45,500 galaxies (avoiding edge-on disks) in several stellar mass bins, finding a double Sérsic to be a good fit to the observed profiles. There have also been claims that the surface brightness profiles of elliptical galaxies are better represented by three components (Huang et al. 2013), with radii of $< 1$ $R_e$, $\sim 2.5$ $R_e$, and $\sim 10$ $R_e$, all with Sérsic values of $n \sim 1$–2. Thus, a range of radii from much smaller than 1 $R_e$ to 8–10 $R_e$, has been reported in the literature as key transition radii. Very few studies have quantified the transition radius between different galaxy components and the mass associated with each component. This has, however, been attempted by Spavone et al. (2017) and Spavone et al. (2020), using deep imaging of ETGs from the VEGAS survey. Fitting double Sérsic functions to the galaxy surface brightness profiles and deriving transition radii from this they inferred outer halo mass fractions, finding evidence for higher-mass fractions in the outer component for more massive galaxies.

We note that several late-type galaxies (LTGs) have been studied in order to measure their outer halo light, e.g., the deep imaging of Merritt et al. (2016) using the Dragonfly camera. This study revealed a large range in the fraction of halo light in LTGs beyond five disk scale lengths from $\sim$10% to $<$0.01%. However, it is not clear to what extent this represents the accreted component of the disk galaxies as this outer light could also come from extended thick disk components, and thus is not necessarily a measure of the ex-situ fraction of the galaxies.

In this work, we investigate the in-situ and accreted components using galaxies from the hydrodynamical cosmological simulation Magneticum. We compare their total and radial accretion properties to results from other cosmological hydrodynamical simulations as well as to observations of massive ETGs, especially addressing the question of to what extent the transition radii from accreted to in-situ components can be inferred from Sérsic fits to the radial mass surface density profiles. In Section 2 we present the simulations and the details of our classification of in situ and accreted. Results from our simulations are presented in Section 3. This includes the classification of the 3D radial density profiles into six classes (Section 3.1), probing their assembly history (Section 3.2), a comparison with other simulations (Section 3.3), and a study of the correlation of the in-situ/accreted fractions with various galaxy properties (Section 3.4) and the transition radii (Section 3.5). In Section 4 we fit the projected mass density profiles with (double) Sérsic fits as commonly done in observations. In Section 5 we provide a comparison of these 2D mass density profiles of ETGs from simulations with observations and examine whether outer halo mass fractions correspond to true fractions of accreted material. Finally we present our summary and conclusions in Section 6.

[3] For an analysis of the effect of two-body scattering in the presence of particle species of different mass in simulations on galaxy sizes, see Ludlow et al. (2019), which could be an additional caveat for all the simulations.

## 2. The Magneticum Pathfinder Simulations

We use the Magneticum Pathfinder[4] simulations (Hirschmann et al. 2014; Ragagnin et al. 2017; K. Dolag et al., in preparation), which are a set of cosmological hydrodynamical SPH simulations of several boxes with volumes ranging from $(2688\ \mathrm{Mpc}/h)^3$ to $(48\ \mathrm{Mpc}/h)^3$ and with different resolutions, the lowest having $m_{\mathrm{Gas}} = 2.6 \times 10^9\ M_\odot/h$ and the currently highest having $m_{\mathrm{Gas}} = 7.3 \times 10^6\ M_\odot/h$. Each gas particle can spawn up to four stellar particles during its lifetime, and as such, the average mass of a stellar particle is 1/4 of the gas particle for each resolution. A WMAP7 ΛCDM cosmology (Komatsu et al. 2011) is adapted throughout all simulations, with $\sigma_8 = 0.809$, $h = 0.704$, $\Omega_\Lambda = 0.728$, $\Omega_{\mathrm{M}} = 0.272$, $\Omega_{\mathrm{B}} = 0.0451$, and an initial slope for the power spectrum of $n_{\mathrm{s}} = 0.963$.

All simulations are performed with a version of GADGET-3 that includes various updates in the formulation of SPH (Dolag et al. 2004, 2005; Donnert et al. 2013; Beck et al. 2016) as well as in the subgrid physics, especially with respect to the star formation and metal enrichment descriptions (Tornatore et al. 2004, 2007; Wiersma et al. 2009) and the black hole feedback (Fabjan et al. 2010; Hirschmann et al. 2014). For more details on the physics included in the Magneticum Pathfinder simulations we refer the reader to Hirschmann et al. (2014); Teklu et al. (2015) and Dolag et al. (2017). Individual halos and their galaxies are identified using a modified version of SUBFIND (Springel et al. 2001; Dolag et al. 2009).

As shown in previous works, the Magneticum Pathfinder simulations successfully reproduce several observational results over a broad range of masses, from galaxy clusters down to field galaxies. Most relevant for the work presented here, they successfully capture the evolution and properties of black holes (BHs) and AGN (Hirschmann et al. 2014; Steinborn et al. 2015, 2016; Biffi et al. 2018), the angular momentum properties (Teklu et al. 2015), the kinematic properties within the half-mass–radius (Schulze et al. 2018) and in comparison with other simulations and observations (van de Sande et al. 2019), and the dynamical properties of galaxies such as the dark-matter fractions and density profiles (Remus et al. 2017; Teklu et al. 2018) at low and high redshifts. More specifically, Teklu et al. (2017) provide the stellar-mass–halo-mass relation and the baryon fractions for the box volume used in this work, showing that both are successfully reproduced in comparison with observations and models. Especially relevant for the work presented in this paper, the Magneticum spheroidal and disk galaxies successfully match the observed mass–size relation up to redshifts of $z = 2$ (Remus et al. 2017; Schulze et al. 2018). Furthermore, Harris et al. (2020) provide a comparison of the dark-matter fractions and mass–size relations for different box volumes in comparison with observations, while Lotz et al. (2021) provide phase-space properties for galaxies in cluster environments for different box volumes, showing good agreement between the different resolutions and box sizes. And while quenched fractions for the box volume used in this work are currently only available for ETGs from $z = 2$ to present day (Remus et al. 2017), quenched fractions for the larger box volume in comparison to other simulations are provided by Corcho-Caballero et al. (2021).

[4] www.magneticum.org

### 2.1. High-resolution Simulation

As we are focusing on the internal properties of galaxies in this work, we use the currently largest volume of Magneticum with the highest resolution level available. This box has a size of $(48\ \mathrm{Mpc}/h)^3$. It initially contains a total of $2 \times 576^3$ (dark-matter and gas) particles. The mass resolution for the dark-matter, gas, and stellar particles is $m_{\mathrm{DM}} = 3.6 \times 10^7\ M_\odot/h$, $m_{\mathrm{Gas}} = 7.3 \times 10^6\ M_\odot/h$, and $m_* \simeq 2 \times 10^6\ M_\odot/h$, respectively, with a softening of $\epsilon_{\mathrm{DM}} = \epsilon_{\mathrm{Gas}} = 1.4\ \mathrm{kpc}/h$ for dark-matter and gas particles, and $\epsilon_* = 0.7\ \mathrm{kpc}/h$ for stellar particles.

We choose a lower total halo mass limit of $M_{\mathrm{vir}} \geqslant 5 \times 10^{11}\ M_\odot$, resulting in a stellar-mass limit of $M_* \geqslant 10^{10}\ M_\odot$, with the caveat that some galaxies with $M_* \geqslant 10^{10}\ M_\odot$ are discarded as they do not fulfill the total mass criterion, to ensure sufficient resolution for radial density profile fits and to measure in-situ/ex-situ mass fractions. We additionally limit the sample to central galaxies to ensure proper treatment of the in-situ/ex-situ classification. The highest mass galaxies in this simulation are $M_* \sim 10^{12}\ M_\odot$. With these restrictions, we select 511 galaxies, which include four galaxies that are BCGs, and 43 galaxies that are brightest group galaxies.

### 2.2. Definition of Accreted and In-situ Stars, and Stellar Mass

We are interested in the accreted (ex-situ) and the in-situ components of the galaxies. Therefore, we have to trace all stars that are part of a galaxy at $z = 0$ back to their formation redshift. If a star is born inside the main-branch progenitor of the galaxy, it is considered to be formed in situ. If a star was born outside the virial radius of the main-branch progenitor of the galaxy, and only later in its life accreted onto that galaxy, then it is considered to be "accreted" independent of whether it was accreted smoothly or as part of another galaxy. If a star particle is born inside the virial radius of the main-branch progenitor but in the wake of a gas-rich merger, we still consider the star to be formed in situ, as otherwise all stars would be accreted since, ultimately, all gas has been accreted onto the galaxy. These stars have been handled differently in the literature, however, for the sake of a clean classification with respect to the accreted, or ex-situ, fraction we use the classification described above. This gives us the smallest possible fraction of accreted stars and the largest possible fraction of in-situ formed stars. We define the in-situ and ex-situ fractions as the total mass of stars formed in-situ or ex-situ, respectively, as described above, relative to the total stellar mass of the galaxy. The total stellar mass ($M_*$) includes all stars within 10% of the galaxy's virial radius, with the substructures identified by SUBFIND subtracted. Similarly, the half-mass–radius is the radius that contains half of this stellar mass $M_*$. The radial density profiles for the largest galaxies can reach beyond the 10% $R_{\mathrm{vir}}$. However, the stellar mass beyond 10% $R_{\mathrm{vir}}$ is negligible for the mass range probed in this work (only for BCGs is there significant contribution at such large radii). This has been shown already by Harris et al. (2020) for the Magneticum simulations, and thus we continue with the commonly used definition of stellar mass and half-mass–radius within 10% $R_{\mathrm{vir}}$.

### 2.3. Galaxy Classification

The sample of 511 Magneticum galaxies includes all galaxy types. However, in the second part of this study, we partially

**Table 1**
Profile Classes for All 511 Galaxies from the Magneticum Simulation Used in this Work

| Class | All | | Spheroidals | | Disks | |
|---|---|---|---|---|---|---|
| | *N* | % | *N* | % | *N* | % |
| Class A | 36 | 7.1 | 15 | 9.7 | 1 | 0.95 |
| Class B | 9 | 1.8 | 6 | 3.9 | 1 | 0.95 |
| Class C | 367 | 71.8 | 100 | 64.9 | 78 | 74.3 |
| Class D | 66 | 12.9 | 24 | 15.6 | 18 | 17.1 |
| Class E | 19 | 3.7 | 7 | 4.6 | 2 | 1.9 |
| Class F | 14 | 2.7 | 2 | 1.3 | 5 | 4.8 |

**Note.** The sample includes 154 early-type spheroidal galaxies, 105 late-type disk galaxies, and 252 intermediate type.

restrict our investigation to spheroid-dominated (or early-type) galaxies due to the fact that most observations we can compare to are based on ETGs. We classify the galaxies using the $b$-value

$$b = \log_{10}\left(\frac{j_*}{\text{kpc km s}^{-1}}\right) - \frac{2}{3}\log_{10}\left(\frac{M_*}{M_\odot}\right),$$

which effectively gives a galaxy's position in the $M_*$–$j_*$ plane as discussed by Teklu et al. (2015). At $z = 0$, galaxies with a $b$-value of $b \leqslant -4.73$ are spheroid-dominated (which we refer to as ETGs), while galaxies with $b \geqslant -4.35$ are classified as disks or LTGs (Teklu et al. 2017). Galaxies with $b$-values in between these limits have intermediate properties, i.e., they include galaxies with both bulge and disk components, but also a small number of ongoing-merger and interacting galaxies. This is the same classification that has been used by Teklu et al. (2017), Schulze et al. (2018), and Schulze et al. (2020). On this basis our sample includes 154 ETGs, 105 disk galaxies, and 252 intermediate galaxies.

## 3. Accreted and In-situ Formed Stars in Magneticum Galaxies

### 3.1. Radial Stellar Mass Density Profiles

We calculate the radial stellar mass density profiles for the Magneticum galaxies using equal particle bins with at least 200 particles per bin, in spherical shells around the galaxy center. For the in-situ and the accreted components, the same radial bins are used as for the total profile to ensure a direct radial comparability of the two components. While the profiles reach further in than 1.4 kpc, which corresponds to twice the softening length, we do not use those inner regions for the classifications in the following.

Inspecting the 3D radial stellar density profiles (in $M_\odot/\text{kpc}^3$) of the Magneticum galaxies, we find six different classes based on their in-situ/accreted behavior. The results are summarized in Table 1. Examples for each class are shown in Figures 1 and 2, and 3, and described in the following:

1. Class A: Extremely accretion-dominated profiles. For these galaxies, the accreted stellar component is always dominant, even in the inner regions (see left panels of Figure 1 and upper left panels of Figure 3). About 7% of all galaxies show this kind of behavior (see Table 1). Such galaxies have no clear transition radius between in-situ and accreted stellar mass.
2. Class B: Accretion-dominated profiles. For these galaxies, the fraction of in-situ and accreted stars near the galaxy center is equal, but for all larger radii the accreted fraction dominates (see middle panels of Figure 1 and upper right panels of Figure 3). This is a rare class, with only about 2% of all Magneticum galaxies in this class (see Table 1). It could also be interpreted as an extreme case of class A, but we here study it as a separate class. The transition radius for these galaxies is very small, and is not a real transition in all cases as the in-situ component does not necessarily dominate in the center but sometimes is simply equal amounts of in situ and accreted.
3. Class C: Classic profiles. The inner regions of these galaxies are dominated by in-situ formed stars, while in the outskirts the accreted stellar component is dominant (see right panels of Figure 1 and central left panels of Figure 3). This is by far the most common class of profiles, with 72% of all Magneticum galaxies showing this behavior (see Table 1). This is also the behavior found most commonly in previous work for example by Cooper et al. (2010); Rodriguez-Gomez et al. (2016); Pulsoni et al. (2021). These galaxies have a clear transition radius from in-situ to accretion dominated.
4. Class D: Double cross-over profiles. These galaxies have a large accreted fraction dominating the inner and the outer regions, with their intermediate-radii regions dominated by in-situ formed stars (see left panels of Figure 2 and central right panels of Figure 3). 13% of all Magneticum galaxies fall in this category (see Table 1), making this the second most common profile type. Given their nature, these profiles have two transition radii.
5. Class E: Balanced profiles. A small fraction (≈4%, see Table 1) of all Magneticum galaxies reveal profiles for which the in-situ and accreted contributions are nearly equal over a large radial range (see middle panels of Figure 2 and bottom left panels of Figure 3). For these profiles, we usually find a transition radius at very large radii, however, even if the outer parts are slightly dominated by accreted stars, the fraction of accreted stars usually stays below 60%.
6. Class F: In-situ-dominated profiles. Galaxies in this class have radial density profiles that are always dominated by in-situ formed stars at all radii, even at their outskirts (see right panels of Figure 2 and bottom-right panels of Figure 3). Only 2.7% of all Magneticum galaxies show this behavior, with the in-situ fraction always larger than the accreted fraction (Table 1). As for class A galaxies, there is no transition radius for these galaxies.

Recently, a similar analysis of radial in-situ and accreted profiles in ETGs has been presented by Pulsoni et al. (2021) using the IllustrisTNG simulations. Different from our six classes of 3D mass density profiles, they reported four classes based on 2D mass surface density profiles: Their class 1 (20% of the sample) galaxies are in-situ dominated at all radii, equivalent to our class F galaxies, although our class F only covers 2.7% of all galaxies and only 1.3% of those that are classified as spheroidals. Class 2 is their most common profile (57%), and is equivalent to our class C, although we have more galaxies of class C (72% of all galaxies and 65% of our ETGs). This is also the only kind of in-situ/accreted profile that has been reported for Illustris galaxies

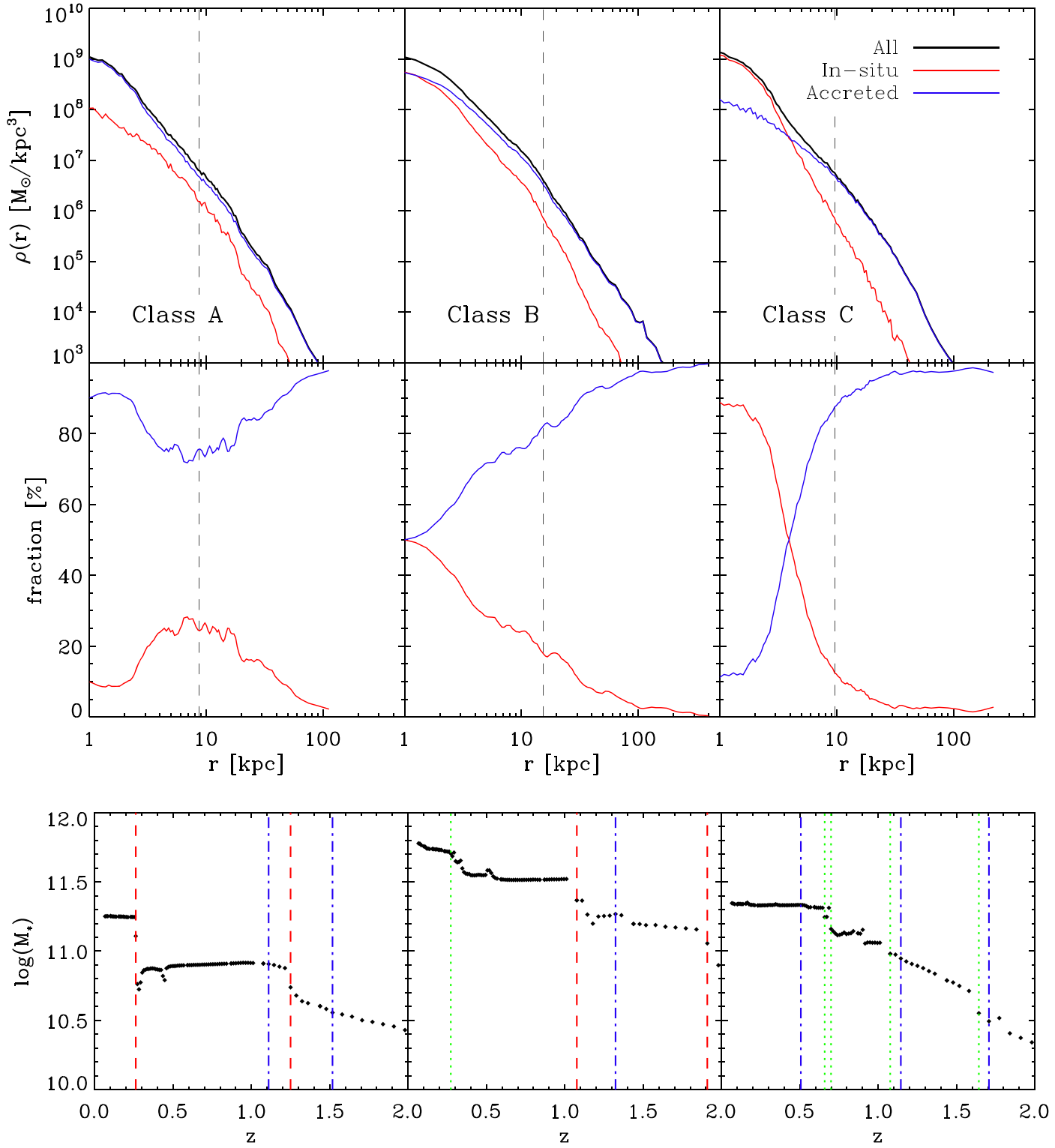


**Figure 1.** Examples for three of the six different in-situ/accreted profile classes, from left to right: class A (extremely accretion dominated), class B (accretion dominated), and class C (classic). The vertical black dashed lines in the upper panels indicate the half-mass–radius. Upper panels: radial stellar density profiles for all stars (black lines), in-situ formed stars (red lines), and accreted stars (blue lines). Middle panels: relative mass fractions of the in-situ (red) and accreted (blue) subcomponents. Bottom panels: the assembly history of the stellar mass of the example galaxies. Dashed red lines show major mergers (mass ratios of 1:1–3:1), green lines show minor mergers (mass ratios of 3:1–10:1), and blue lines show mini mergers (mass ratios below 10:1).

(Rodriguez-Gomez et al. 2016). Their class 3 (15%) is closest to our double cross-over profiles (class D), and with 13% of our galaxies being class D the numbers are very similar between the two simulations, even better matched if we only compare with our spheroidals (15.6%). Their class 4 galaxies are accretion dominated and their least common profile at 8%. In our work such profiles were divided into class A (extremely accretion dominated) and B (accretion dominated), representing a total of about 9% of galaxies and 13% for the spheroidals alone, again in good agreement. We also classified ∼4% of our

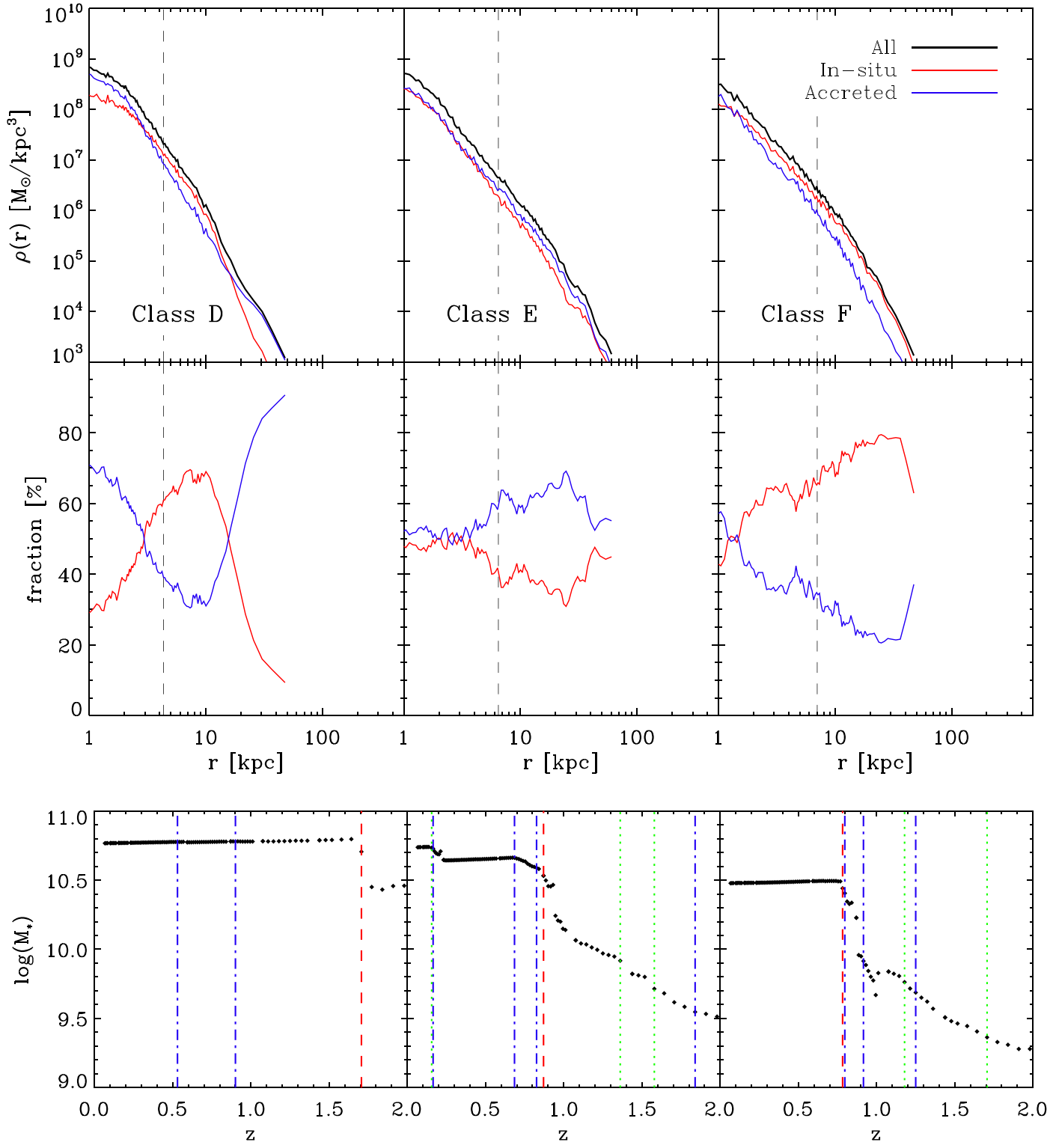


**Figure 2.** Same as Figure 1 but for the other three profile classes, from left to right: class D (double cross over), class E (balanced), and class F (in-situ dominated).

galaxies to be "balanced" with similar in-situ and accreted components, a class that does not appear in the classifications by Pulsoni et al. (2021).

To summarize, the main differences are that we find more classic profiles (72% versus 57%) and fewer in-situ-dominated profiles (2.7% versus 20%), clearly highlighting the intrinsic differences between the simulations. We caution the reader, however, that the relative proportions found for each profile class strongly depend on the selection used to classify ETGs (which is different for both simulations), and also on the mass range covered in those simulations. More explicitly, the IllustrisTNG simulation has a higher resolution and therefore can resolve lower-mass galaxies than those included in this study.

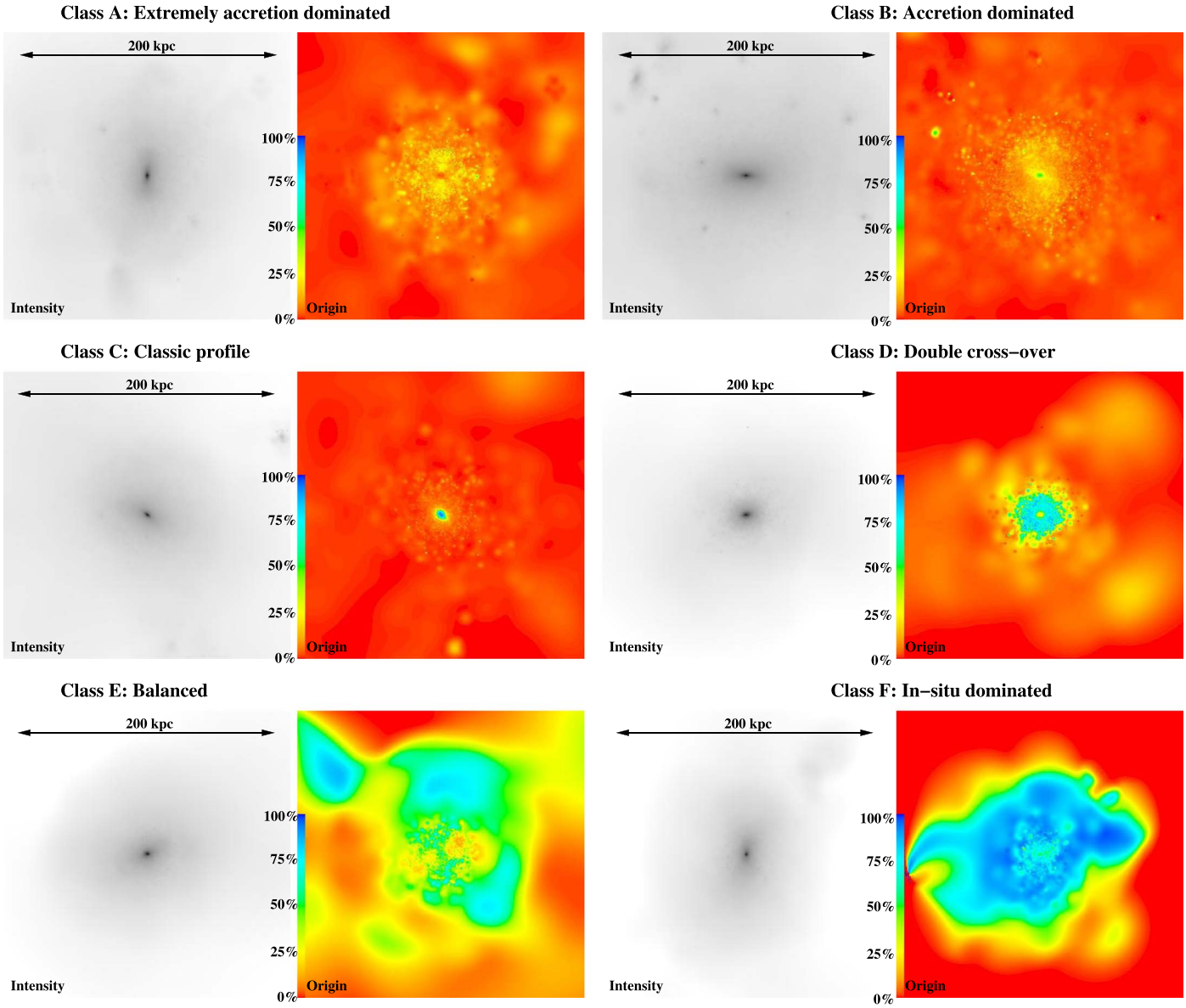


**Figure 3.** Random 2D projected views of the example Magneticum galaxies for each of the six profile classes. For each galaxy, a box with a length of 200 kpc centered on the galaxy is shown, with the left plot showing the intensity map derived from all stars in the galaxy and the right plot showing the origin of the stars, color coded according to the in-situ/accreted fraction (with blue colors showing 100% in-situ fractions and red colors showing 100% accreted fraction). From left to right, top to bottom, the shown galaxies are from class A (extreme accretion; upper left), class B (accretion; upper right), class C (classic; central left), class D (double cross over; central right), class E (balanced; bottom left), and class F (in situ; bottom right). As can be clearly seen, the amount of in-situ stars increases from the upper left class (A) to the lower right class (F).

### *3.2. Assembly History*

One of the first steps to understanding the origin of the different profile classes is to test whether they correlate with the stellar mass of the galaxy. In the left panel of Figure 4 we show the normalized distribution of the individual profile classes as a function of stellar mass. We find a clear trend that galaxies of classes E and F, where the in-situ component is 50% or larger, are always galaxies with relatively low stellar masses, while galaxies of classes A and B, which are everywhere accretion dominated, usually reside at the high-mass end. This mass trend is expected, as more massive galaxies have generally accreted more mass than low-mass galaxies. Similar trends were seen by Pulsoni et al. (2021) in their study. Interestingly, the two most common classes of galaxies, namely classes C and D, are most likely to be found in the middle mass range of our galaxy sample, with the galaxies having stellar masses of $10.5 < \log(M_*) < 11$. This indicates that it is not the frequency of mergers, but the type of merger that is crucial in establishing the differences.

To understand this in more detail, we study the assembly history of all galaxies with respect to their main formation branch from $z = 2$ to $z = 0$. We distinguish three different kinds of mergers:

1. Major mergers with stellar mass ratios of 1:1–3:1.
2. Minor mergers with stellar mass ratios of 3:1–10:1.
3. Mini mergers with stellar mass ratios below 10:1.

For the mini mergers, there is no lower mass limit in general; however, due to the resolution limit of the simulation, the

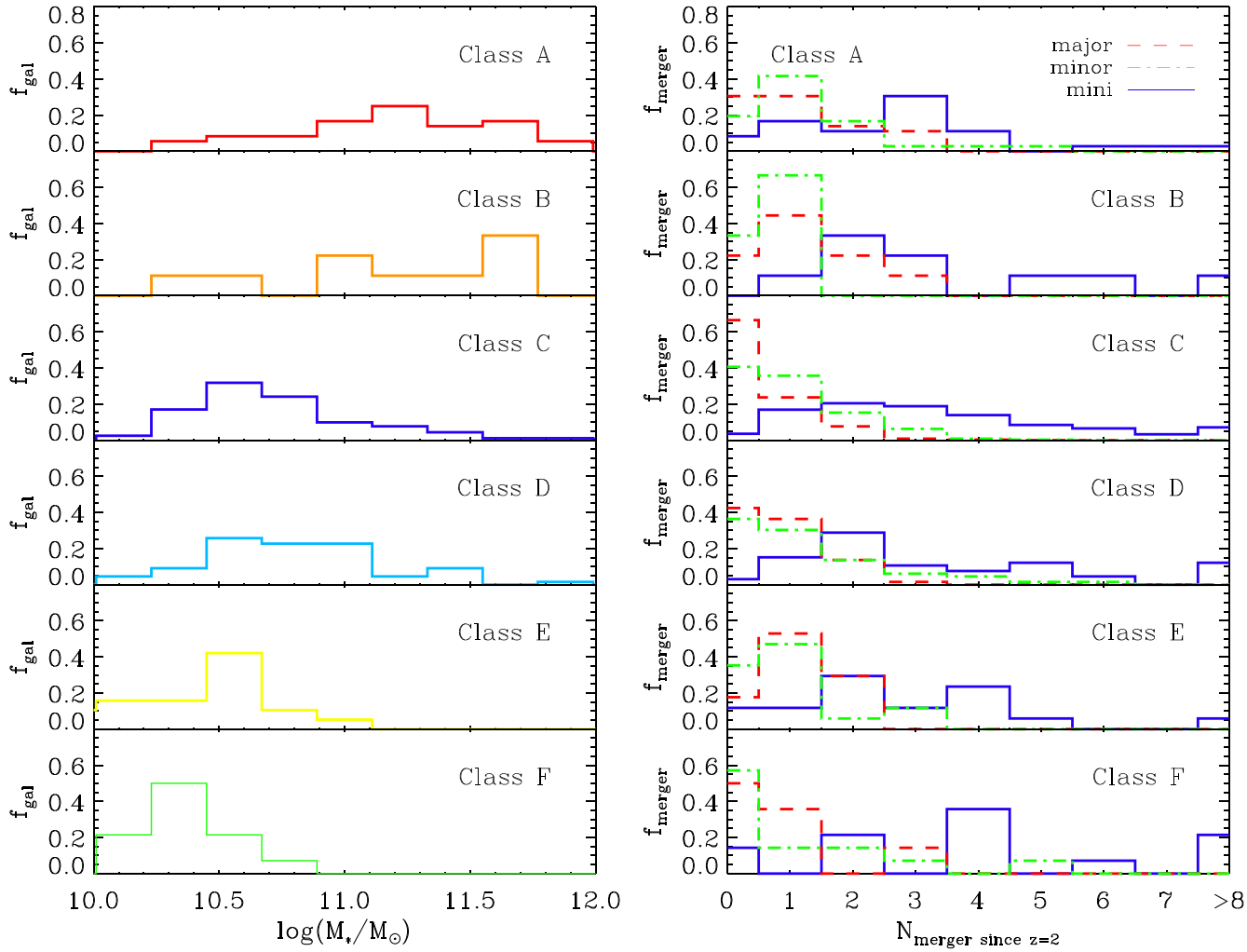


**Figure 4.** Profile class dependence on stellar mass and merger frequency. Histograms are shown as a fraction of the total number in each class. Left panel: histogram of the stellar mass distribution, color coded by profile class. Low-mass galaxies are dominated by classes C, E, and F, while classes A and B are common for high-mass galaxies. Right panels: histogram showing the frequency of major (red), minor (green), and mini (blue) mergers since $z = 2$ for each class. Major mergers are least common for galaxies of class C, where nearly 60% of the galaxies have had no major merger since $z = 2$.

smallest mergers that we can resolve here are on the order of 100:1 in mass ratio. Below this limit, we do not call accretion events mergers, even for those few cases where this would still be resolvable, for the sake of completeness in numbers. Note that this is also the reason why we only consider mergers up to $z = 2$. At higher redshifts, the main galaxies are not that massive yet, and thus many of the mergers have so little stellar mass that we cannot classify mini (or even minor) mergers confidently. For the merger histories below $z = 2$, this is not an issue as mini mergers have sufficient stellar mass to lie above the chosen stellar-mass cuts.

Major mergers are known to have strong impacts on the main progenitor galaxy at all radii, however, this is not in general the case for minor and mini mergers. While minor mergers, especially in the mass range around 5:1, can still strongly influence the mass distribution of the progenitor galaxies even at their centers (e.g., Hilz et al. 2013; Karademir et al. 2019), mini mergers mostly contribute to the outer halos of galaxies and only play a role for the central evolution of the host galaxy for radial infall orbits or head-on collisions (Karademir et al. 2019). Since we focus on radial ranges beyond the half-mass–radius, all types of mergers can play a role in establishing the different profile classes.

Examples of the assembly history for the six classes are given in the lower panels of Figures 1 and 2, with the history always belonging to the galaxy for which the radial density profiles are shown in the upper panels of the same figures, and the intensity maps are shown in the corresponding panels of Figure 3. The redshifts of past merger events are marked as red/green/blue dashed lines for major/minor/mini mergers, respectively. These six examples show that all galaxies, but one, experience major mergers, with the galaxy that experiences no major merger being of class C. In the case of the example galaxies from classes A and B (the accretion-dominated profile classes), both show two major merger events since $z = 2$. Interestingly, the galaxy from class F, which is dominated by in-situ stars at all radii, experiences a major merger at a redshift of about $z = 1$.

More quantitatively, in the right panel of Figure 4 we show for each profile class histograms of the frequency of major (red dashed lines), minor (green dashed–dotted lines), and mini mergers (blue solid line) since redshift $z = 2$ ($\sim$10 Gyr in look-back time). Furthermore, Figure 5 shows the amount of stellar mass relative to the present-day stellar mass that was accreted through the mergers of different mass ratios and through all mergers for each accretion class in the upper panel, while the

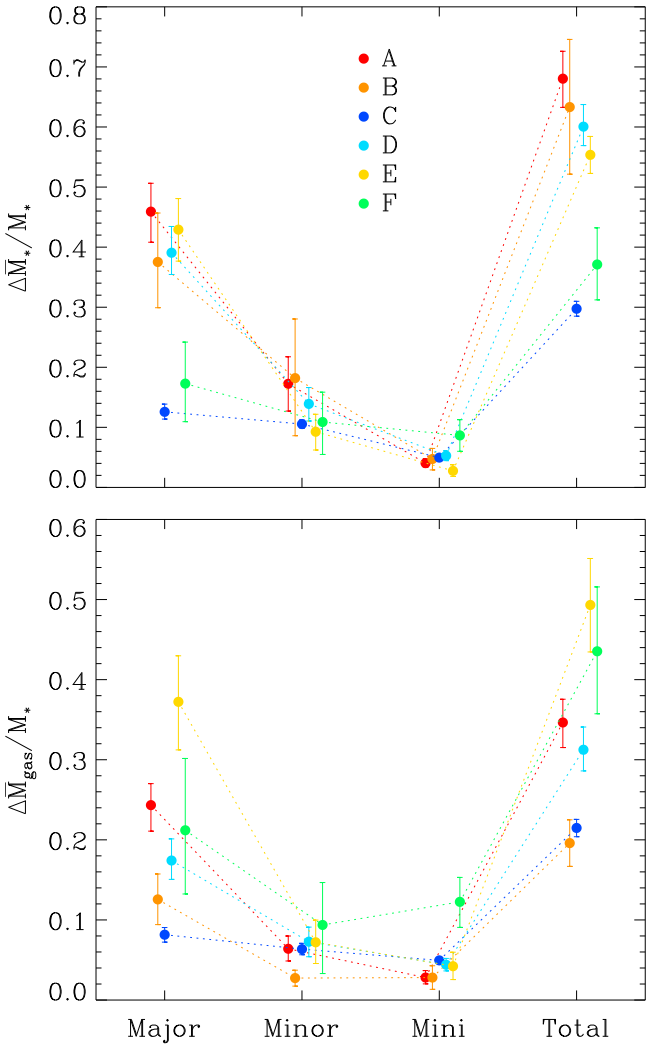


**Figure 5.** Mass fraction added via major, minor, and mini mergers, and all mergers together since $z = 2$ for the six different profile classes. Classes A/B/C/D/E/F are given as red/orange/blue/cyan/yellow/green filled circles, respectively. Top panel: fraction of stellar mass accreted through mergers of different types. Bottom panel: fraction of gas mass accreted through mergers of different types. Gas mass includes hot and cold gas. For the most massive galaxies, a significant fraction of the gas is in a hot (and thus not star-forming) phase. The small shifts for the values on the $x$-axis between the profile classes are purely artificial for visual separation.

lower panel shows the fraction of gas relative to the present-day stellar mass accreted through these mergers for the different accretion classes.

In general, about half of all Magneticum galaxies have experienced at least one major merger since $z = 2$. However, when considering individual profile classes, we find large differences. Most strikingly, major mergers generally play a significant role in the formation of galaxies from accretion classes A, B, D, and E, while they only play a minor role in the evolution of galaxies from accretion classes C and F. This reflects what could already be seen from the example cases, but more statistically we find the following accretion history patterns for our six accretion profile classes:

1. Class A: The accretion history of this "overmerged" class of galaxies is not surprisingly completely dominated by merger events, with a total of nearly 70% of the present-day stellar mass being accreted (see the upper panel of Figure 5). Surprisingly, these mergers are not necessarily dry. Especially the major mergers contribute an average of 25% of the total stellar mass in gas, but the sheer amount of accreted stellar mass is enough to dominate the final galaxy at all radii. Overmerged here does not imply that these galaxies had more mergers in general than other galaxies, or an early formation history, but rather that the mini and minor merger events were unusually dry. This is in good agreement with what we also see from Figure 5, with the minor mergers specifically contributing about 20% in stellar mass growth, while the accreted gas amounts to less than 10% of the total stellar mass. Additionally, most of these galaxies are rather massive, and as such a larger amount of the gas will be present as a hot gas halo and not participate in the star formation process. Galaxies of this profile class are rather common for the spheroidals, but only one of these is found among the disk galaxies.[5]
2. Class B: Galaxies from this accretion class have a similar accretion history to galaxies of class A, with more than 60% of their stellar mass being accreted. The main difference here is that the mergers were all gas poor, resulting in the lowest amount of gas accreted since $z = 2$ in the whole sample (see lower panel of Figure 5).
3. Class C: The "classic" profile shows significantly different behavior from all the others, namely 2/3 of the galaxies in this class have never experienced a major merger since $z = 2$ (see right panel of Figure 4). Even those class C galaxies with major mergers only get about 10% of their mass from this pathway, implying that the major mergers happen rather early for this class (see the upper panel of Figure 5). In general, galaxies of this class only accrete about 30% of their stellar mass through mergers, which is the lowest fraction found for all classes. Furthermore, the mass accreted through the major and minor mergers is approximately equal, and the relative contribution of the mini mergers is rather large for galaxies of this group. This clearly shows the importance of minor and mini mergers in the assembly history of class C galaxies. In addition, we find that the mergers that a galaxy of class C experiences are usually rather dry, and contribute only about 20% of the total stellar mass in gas (see lower panel of Figure 5). This also explains the dominance of the accreted material at large radii and the dominance of the in-situ components in the center, as the minor and mini mergers, especially when dry, often do not reach the central parts of the host galaxy at all but rather deposit their mass at large radii (Purcell et al. 2007; Amorisco 2017; Karademir et al. 2019).
4. Class D: Major mergers are important for half of the galaxies in this profile class, but those mergers are relatively dry (gas poor). The host galaxy, on the other hand, is relatively wet (gas rich) at the time of merging, and through the merger the gas is moved outwards into a ring-like structure, where the star formation occurs. This profile class is equally common for both disks and spheroidals (see Table 1).
5. Class E: The mass accretion history of galaxies from this class is dominated by a single merger which is either a

[5] This is a very special case in which the accretion occurs along a plane along the galaxy's disk plane, similar to what was discussed for mini mergers by Karademir et al. (2019).

major merger (60%) or a massive minor merger (see right panels of Figure 4). These mergers were gas rich, causing a starburst after accretion, which effectively leads to this special profile case where the in-situ and accreted radial fractions are identical over a broad radial range. As known from classical binary merger simulations (e.g., Hernquist & Barnes 1991), these mergers usually result in a spheroidal galaxy as long as the merger is not in-plane or has a very high gas fraction (Springel & Hernquist 2005). This is reflected in the low fraction of disk galaxies in this class (only 1.9%), while for the spheroidals they account for 4.6%, as seen in Table 1.

6. Class F: Galaxies of class F show similar behavior to galaxies of class C, as only half of them experience a major merger and only about 40% of their stellar mass is accreted (see right panel of Figure 4 and upper panel of Figure 5). The major difference is the amount of gas accreted through the merger events independent of the merger mass ratio: We find that all mergers deliver significantly more gas than for the galaxies of class C, with a total of about 80% of the stellar mass being accreted in gas mass (see lower panel of Figure 5), which is the highest frequency found for the different profile classes. This gas contributes to star formation, resulting in an overall in-situ-dominated radial density profile. This clearly shows that the origin of these overall in-situ-dominated profiles is gas-rich accretion, and as such it is surprising that two of these galaxies are actually spheroidals.

### 3.3. Accreted Mass Fractions and Galaxy Mass

Overall, there is broad agreement between different simulations that seek to model the accretion of stars during the process of galaxy assembly. In particular, they show that the fraction of accreted stars is correlated with the stellar (and halo) mass of galaxies. This has been described extensively in previous studies for a number of the large hydrodynamical cosmological simulation suites: EAGLE (Davison et al. 2020), Illustris (Rodriguez-Gomez et al. 2016), IllustrisTNG (Pillepich et al. 2018; Tacchella et al. 2019), and Horizon-AGN (Dubois et al. 2016). We refer the reader to the original publications for more details.

In the upper two panels of Figure 6 we have compiled the average ex-situ fractions against stellar mass (right panel) and halo mass (left panel) from the simulations listed above, adding the average trend from the Magneticum simulations. As can be seen immediately, there are significant differences between the simulations especially for low stellar and halo masses of around $M_* \approx 2\text{–}3 \times 10^{10}\ M_\odot$ and $M_{200c} \approx 5 \times 10^{11}\ M_\odot$, respectively. The lowest ex-situ fraction at low masses is $\leqslant$5% for the IllustrisTNG simulations, while the highest fractions are $\sim$40% found in the Magneticum simulations. At the high-mass end, all simulations converge to ex-situ fractions of around 70%–80% for galaxies of stellar masses above $3 \times 10^{11}\ M_\odot$ (or halo masses above $1 \times 10^{13}\ M_\odot$).

So while the global trends agree reasonably well between all simulations, there are several possible reasons for the simulations to differ with respect to the actual fractions, especially at the low-mass end: First, each simulation uses different halo finders to identify the galaxies, potentially leading to different stellar masses obtained for the same galaxies. Second, the method of obtaining the ex-situ fractions differs as well: for IllustrisTNG and EAGLE, fixed apertures were used to obtain the ex-situ fractions, while for Illustris, Horizon-AGN, and Magneticum all stars identified by the halo finder were used. As shown by Pillepich et al. (2018), this can lead to differences in the ex-situ fractions of up to 20%.

As we will later compare to observations that are not limited by fixed apertures, we decide to not use apertures but instead use all stars attributed to the galaxy by our halo finder as discussed in Section 2.2. Note that at least for the five large cosmological simulations shown here, the definitions of in-situ and accreted (ex-situ) mass largely agree in that they only count those stars as accreted that were already formed at infall, and count those stars that were formed from accreted gas after the merger event as in situ (see also Rodriguez-Gomez et al. 2016; Tacchella et al. 2019). This means that, effectively, the accreted fractions are lower limits, and the values could only get higher for more elaborate definitions of in-situ and accreted mass.

Finally, the implemented subgrid physics can also substantially change the number of stars formed inside a given halo, and as such lead to different results with respect to the ex-situ fractions (see, e.g., Moster et al. 2020). Here, one of the most crucial components to influence the ratio of accreted to in-situ stars is the implemented stellar and/or AGN feedback, which is modeled slightly differently in each simulation, but is known to have a strong impact on the ex-situ fractions (see, e.g., Hirschmann et al. (2015) for a study of the effect of stellar feedback on the ex-situ fractions, and Dubois et al. (2013, 2016) for a study of the impact of AGN feedback on the amount of accreted stars). As all five fully hydrodynamical simulations shown here include both types of feedback, albeit in different implementations, it is not possible to know which of the processes is the main driver of the differences between the simulations without a detailed analysis. Such an analysis is beyond the scope of the current paper, and here we simply show in Figure 6 the Magneticum simulations relative to the other main simulation suites.

While the differences found for the ex-situ fractions are hampered by the above-mentioned issues of determining stellar masses, the total halo masses are not influenced by them, and thus we also included a comparison for the halo masses and ex-situ fractions in the upper left panel of Figure 6. Here we can only compare to the IllustrisTNG simulations and the results from the particle tagging method used on a dark-matter-only simulation by Cooper et al. (2013). This shows that the average ex-situ fractions at a given mass found for the Magneticum simulations are close to the results found for spheroid-dominated galaxies by Cooper et al. (2013), while the IllustrisTNG results are similar to the results found by Cooper et al. (2013) for disky galaxies.

One possible source of difference between the two simulations could be that their stellar mass–halo mass relations (SMHR) are different. Thus, Figure 7 shows the SMHR for the Magneticum simulation as well as the IllustrisTNG simulation, both for all stars assigned to a halo (but excluding stars assigned to satellite galaxies), and only for those within a 30 kpc aperture. The values for the IllustrisTNG simulations are presented and discussed in detail by Pillepich et al. (2018), while the SMHR for the Magneticum simulations has been discussed already by Teklu et al. (2017). As can be seen immediately, the simulations do not differ strongly in their slope, and both are in overall agreement with the observations

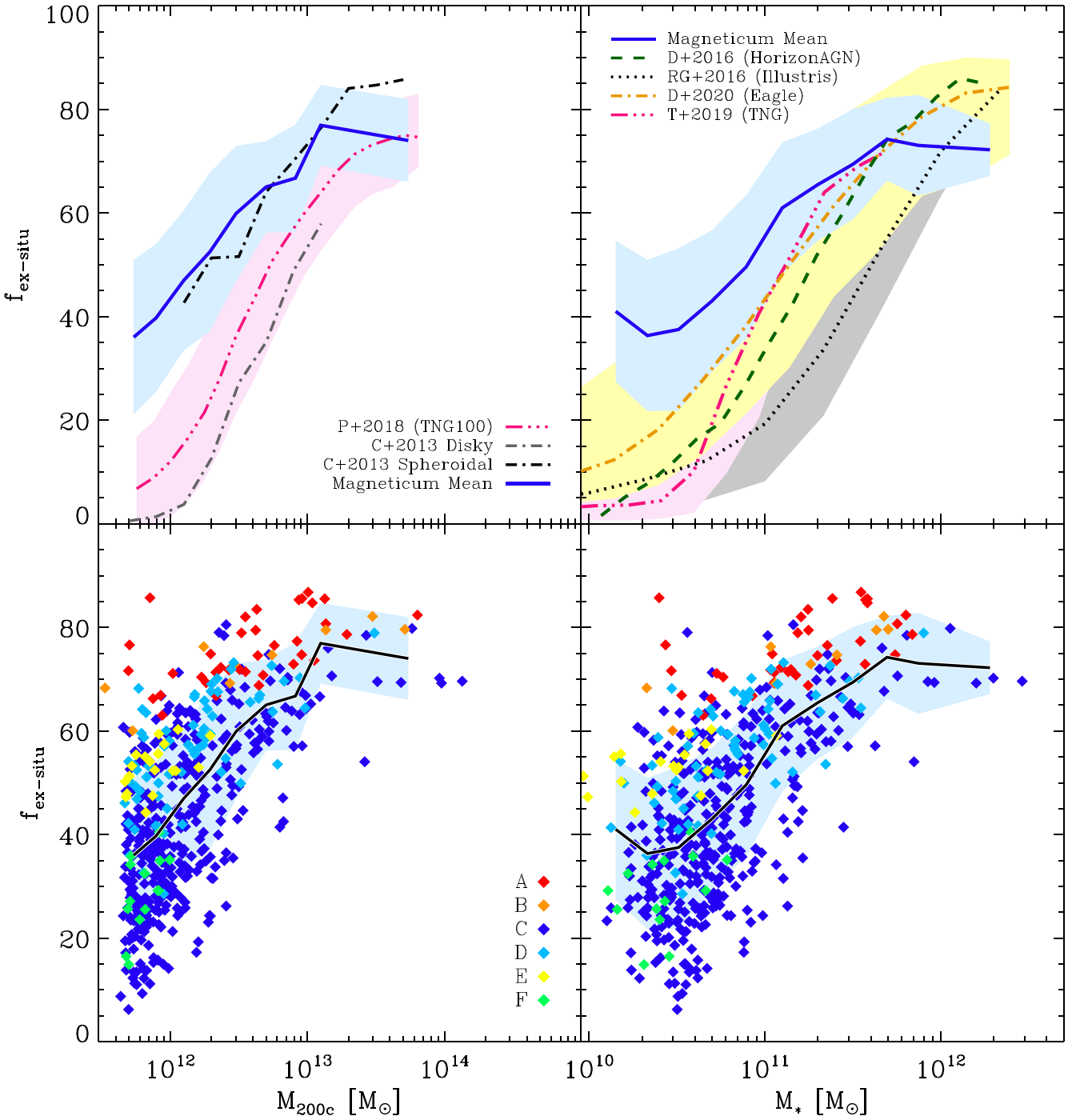


**Figure 6.** Ex-situ (accreted) fractions for Magneticum galaxies in comparison to other simulations. Upper left panel: mean ex-situ fraction vs. critical halo mass $M_{200c}$ for Magneticum (solid blue line), with the $1\sigma$ scatter shown in light blue. For comparison, mean values are also shown for IllustrisTNG100 (Pillepich et al. 2018; dashed–dotted–dotted–dotted pink line and shaded area), and the particle tagging models from Cooper et al. (2013; dashed–dotted lines). Lower left panel: same as the upper panel but showing the individual values for the Magneticum galaxies, with the colors marking the different profile classes as indicated in the legend. The solid line (here black instead of blue for better visibility) and blue shaded area mark the mean and $1\sigma$ scatter for this distribution, as in the upper panel. Upper right panel: ex-situ fraction vs. stellar mass $M_*$. The blue solid line and shaded area show the mean and the $1\sigma$ scatter for the Magneticum galaxies, as in the left panel. For comparison, we include the relations for four other fully cosmological simulations: Illustris (Rodriguez-Gomez et al. 2016; dashed black line and gray shade), Eagle (Davison et al. 2020; yellow dashed–dotted line and yellow shade), IllustrisTNG (Tacchella et al. 2019; pink dashed–dotted–dotted–dotted line and shade), and Horizon-AGN (Dubois et al. 2016; green dashed line). Lower right panel: same as the upper right panel, but for the individual Magenticum galaxies with the colors marking the different profile classes as in the lower-left panel. Again, the Magneticum mean is shown as a solid black line and the blue shaded area marks the $1\sigma$ scatter for this distribution, as in the upper panel. Magneticum galaxies tend to have higher accretion fractions at low masses compared to other simulations.

by Hudson et al. (2015) from weak lensing where an aperture is applied to calculate the stellar mass, but also with the observations by Kravtsov et al. (2018), who presented stellar masses of BCGs both with and without the intra-cluster light (ICL) component included. While the latter data are only available for the very high-mass end, it is clear that the Magneticum simulations are in good agreement with the measurements if the stellar mass is calculated from both

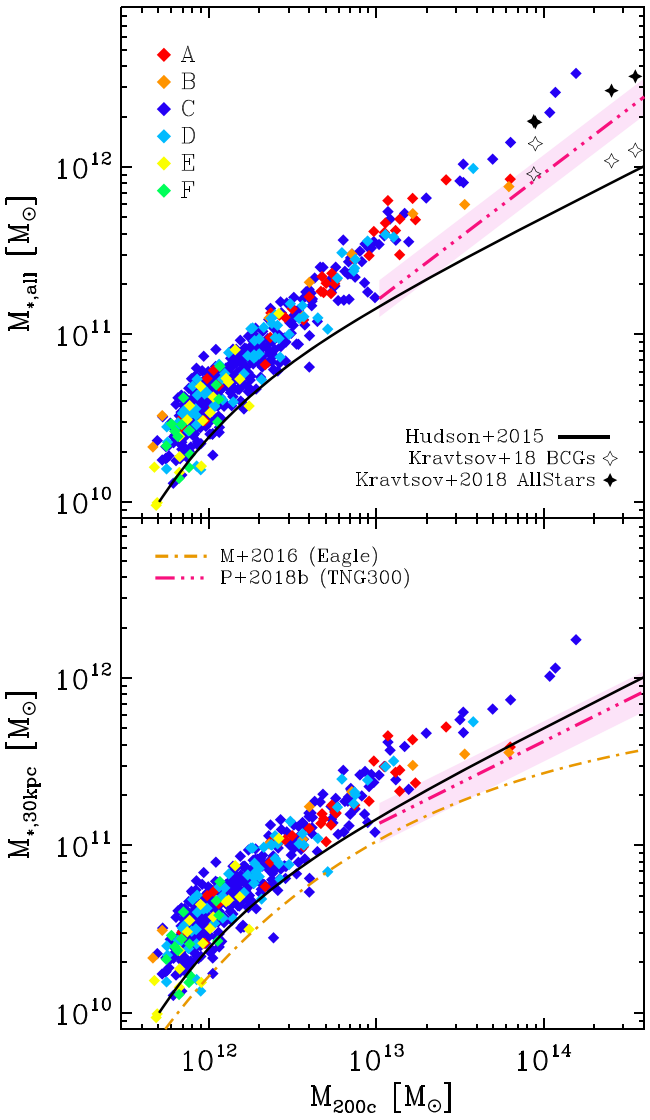


**Figure 7.** Stellar mass–halo mass relation (SMHR) for the Magneticum galaxies in comparison to observations and other simulations. The colors mark the different accretion classes as in the previous figures. Upper panel: stellar mass calculated from all stars assigned to the main halo by SUBFIND, including the outer stellar halos (and the ICL component in case of the BCGs), but excluding satellite galaxies. Lower panel: stellar mass calculated from all stellar particles within a fixed aperture of 30 kpc radius. For the observations, the SMHR determined from weak lensing by Hudson et al. (2015) is included as solid black lines in both panels. In the upper panel only, observations of BCGs by Kravtsov et al. (2018) are included as diamonds, with open diamonds indicating measurements of the stellar mass from BCGs only, while filled symbols mark the same objects but the stellar masses are calculated from BCG plus the ICL component. The latter is comparable to what is done in the simulations. For the simulations, values for IllustrisTNG300 from Pillepich et al. (2018) are included as pink lines and shaded areas in both panels, using the same stellar mass definitions as used for the Magneticum simulations. For the EAGLE simulations, the SMHR is included in the lower panel only, using the stellar mass calculations within 30 kpc from Matthee et al. (2017).

the BCG and ICL components together (see the upper panel of Figure 7). There is, however, a general offset between IllustrisTNG, EAGLE and Magneticum galaxies regarding their stellar mass at a fixed halo mass, indicating that the differences in the ex-situ fractions are most likely driven by the number of stars formed in small galaxies that are later on accreted onto the galaxies, with Magneticum converting larger amounts of gas into galaxies in low-mass halos. However, to really understand the reasons for the differences here, a detailed comparison between the simulations would be required, which is beyond the scope of this work.

So far, we have discussed the mean values of the accreted fractions with stellar and halo mass for the Magneticum simulation in comparison to other simulations. Now we want to take a closer look at the distribution of the individual galaxies with regard to their accretion classes A–F. They are shown in the lower two panels of Figure 6 in comparison to the mean value lines shown in black. As can be seen immediately, there are strong differences between the galaxies of the different accretion classes: The galaxies from the overmerged classes A and B all show high accretion fractions, well above 60%, with no real trend with mass visible. On the other hand, the in-situ-dominated galaxies of class F all have, as expected, low accretion fractions below the mean Magneticum values, and their spread in mass is too small to see any trend with mass for both stellar and halo mass. Similarly, galaxies of the major merger class E also show no trend in mass, and the overall accretion fractions are around 50%. For the other two classes, C and D, we find a clear correlation of the accreted fraction with both stellar and halo mass, with a tendency for the galaxies of class D to be slightly above the mean Magneticum accretion values per mass, and for class C to be slightly below on average. Interestingly, class C also includes the lowest accretion fractions at all mass bins, even lower than the galaxies of the in-situ-dominated class F, clearly demonstrating that the accretion fractions can be really low if most of the accretion is provided by dry minor and mini mergers in the outskirts of a galaxy, while the center is left undisturbed. Looking at the SMHR in Figure 7 again, we do not find a correlation between the galaxies of different accretion classes and their positions in the SMHR, other than the already reported general trend for class A and class B galaxies to occupy the higher-mass end preferentially, and class F galaxies to be rather low mass.

### 3.4. Accreted Mass Fractions and Global Galaxy Properties

In the following, we compare the results for our simulated galaxies with observations. For Figure 8, and the other figures below, we show our full sample (unless stated otherwise) of spheroidal through to disk-dominated galaxies. The observational samples may be restricted to a certain type of galaxy, which we note below if applicable. Quantities may also have been measured in different ways, e.g., observations typically measure half-light rather than half-mass radii. We do not attempt to correct or adjust the observational samples in any way. Thus these caveats should be born in my mind by the reader when comparing observations with our simulation results.

It has been shown already by Remus et al. (2017); Schulze et al. (2018), and Harris et al. (2020) that the Magneticum galaxies successfully reproduce the observed stellar mass–size relations (e.g., GAMA, by Lange et al. 2015), but here we now take a closer look at the different profile classes in this relation (left panel of Figure 8—see also the Appendix for the same figure but with the half-mass radii calculated for a random projection). The overmerged galaxies of classes A and B show only small scatter close to the observed relation over the whole mass range, but due to the fact that they are the by far most common class at high stellar masses, they are also most common among the large galaxies. The classical profile

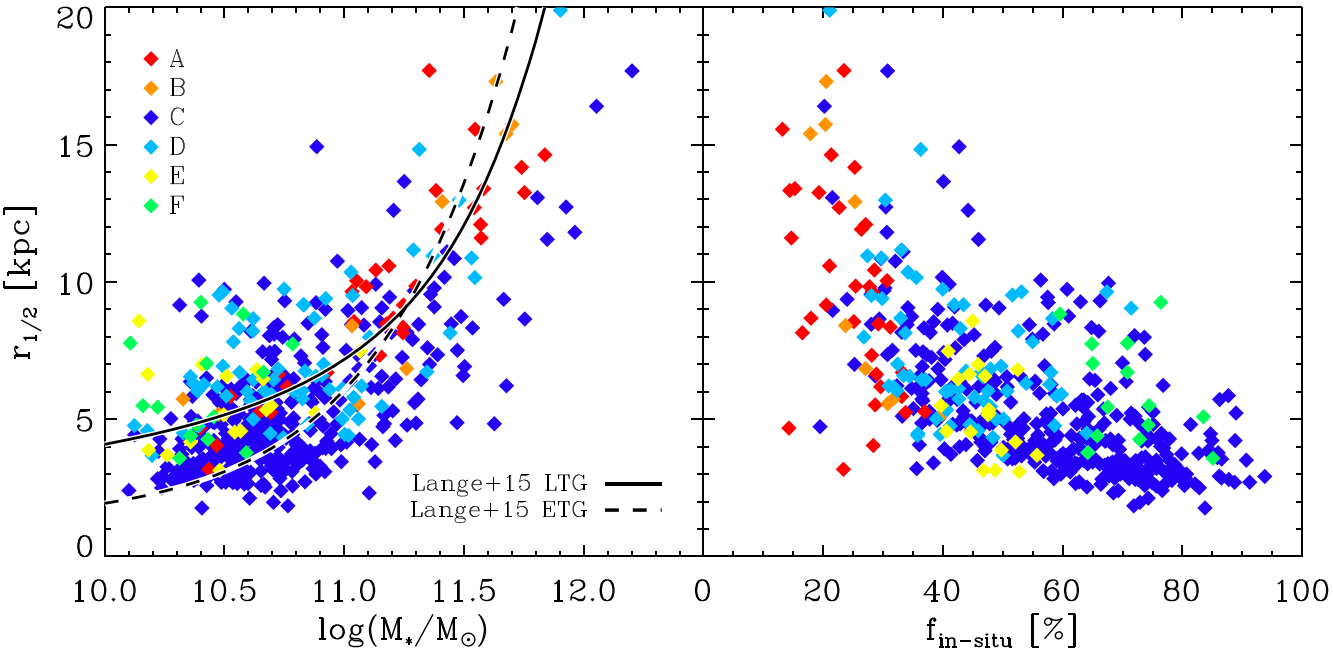


**Figure 8.** Left panel: stellar mass–size relation for all Magneticum galaxies, color coded according to their profile class (see legend). The 3D half-mass–radius is shown against total stellar mass. For comparison, the observed mass–size relation from the GAMA survey by Lange et al. (2015) is shown for ETGs (dashed line) and LTGs (solid line). Note that the observations measure half-light radii instead of half-mass radii. Right panel: in-situ fraction vs. 3D half-mass–radius for the Magneticum galaxies, color coded as in the left panel. Only class C galaxies reveal a clear correlation between in-situ fraction and galaxy size.

galaxies of class C, however, show a significantly different behavior from the galaxies of the other classes, in that they are the clearly dominant class for the small galaxies at all stellar-mass ranges. Although the scatter is large for this class and there are also very large galaxies among them, they clearly dominate the small size end especially at the lower stellar mass end. This reflects our previous findings that these galaxies are dominated by compact star formation in their centers and only little accretion mostly to the outskirts, resulting in a rather compact central part and consequently a smaller half-mass–radius. On the other hand, we see a very different behavior for those galaxies of classes D, E, and F, all of which have large sizes for their stellar masses, clearly dominating the region of the mass–size relation that is usually occupied by disk galaxies. This is in good agreement with the fact that all of them have a large amount of cold gas accreted throughout their formation history since $z = 2$, resulting in in-situ star formation in disks and thus larger half-mass radii (even if in the case of class D galaxies the large central accreted component will prevent its classification as a disk given its massive bulge-like nature).

As stellar mass $M_*$ and 3D half-mass–radius $r_{1/2}$ of a galaxy are correlated, it is not surprising that we also find a correlation between the in-situ fraction of a galaxy and its half-mass–radius (right panel of Figure 8). It can best be seen in the galaxies of accretion class C, as they cover the largest range of both half-mass radii and in-situ fractions, with a clear tendency for smaller galaxies to have larger in-situ fractions and large galaxies to have smaller in-situ fractions. A similar behavior is found for galaxies of classes D and E, although class E only covers such a small range of in-situ fractions that no clear correlation between size and in-situ fraction can be inferred from these galaxies alone. In general, the in-situ fraction decreases with increasing half-mass–radius, i.e., accretion leads to a growth in the scaled size (e.g., Oser et al. 2012). In the case of minor mergers, this is consistent with most of the accreted stars being deposited at large radii (see also Amorisco 2017; Lagos et al. 2018; Karademir et al. 2019; Davison et al. 2020).

For galaxies of the overmerged classes A and B, we find a similarly large range of half-mass radii, but only a small range of in-situ fractions around 20%, and they reveal no correlation at all between size and in-situ fraction. This well reflects the known fact that a major merger results in a much more compact galaxy than a series of minor mergers that bring in the same total mass as the major merger but deposit their masses at different radii (Naab et al. 2009; Hilz et al. 2012). So while all galaxies of these two classes had plenty of mergers, we find the differences in the individual merger mass ratios mirrored in the size distribution. Galaxies of the in-situ-dominated class F show the strongest deviation from the correlation between size and in-situ fraction: while all the in-situ fractions are rather high, the sizes are generally larger than those of the class C galaxies of similar in-situ fraction, in agreement with our previous finding that class F galaxies are more similar to disks than the average class C galaxy.

Finally, we investigate if the fraction of dark matter within the half-mass–radius, $f_{\rm DM}$, is correlated with the in-situ fraction and stellar mass. As can be seen in Figure 9, there is a broad tendency for galaxies with smaller in-situ fractions to have larger central dark-matter fractions, indicating that (massive) accretion events lead to larger fractions of dark matter in the center by either enhancing the relative amount of dark matter in the center or dispersing the baryonic matter. This tendency can be seen for galaxies of all accretion classes but those of class F, the in-situ-dominated class. Galaxies of that class show much higher central dark-matter fractions than galaxies of class C with similar in-situ fractions. This is in good agreement with our previous conclusion that class F galaxies closely resemble the typical behavior of disk galaxies. Observations (e.g., Tortora et al. 2019; Courteau & Dutton 2015) have shown that LTGs have, at the same stellar mass, generally larger central

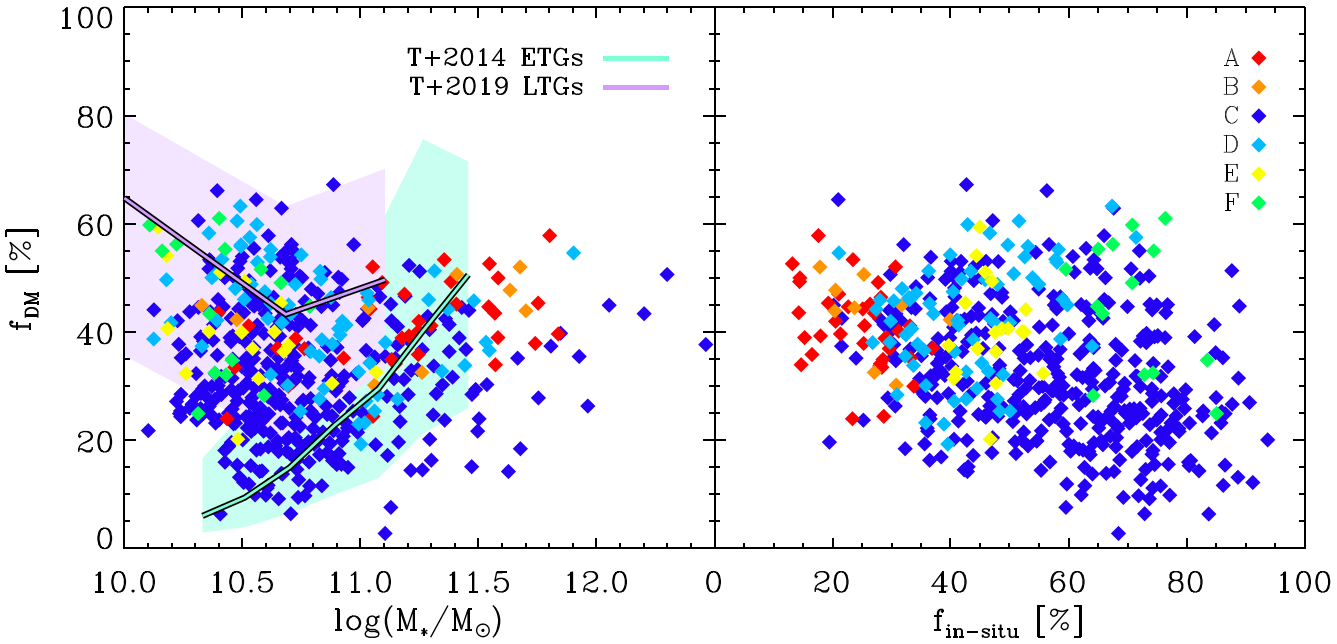


**Figure 9.** Dark-matter fraction within the half-mass–radius trends for all Magneticum galaxies. Left panel: dark-matter fraction $f_{DM}$ vs. stellar mass $M_*$, with colors as in the right panel. Observations for LTGs from the SPARCS survey (Tortora et al. 2019) are included as a lilac solid line and shaded area, and observations for ETGs from the SPIDER survey (Tortora et al. 2014) are included as a cyan solid line and shaded area, with the shaded areas marking the observed $1\sigma$ spread. Right panel: dark-matter fraction $f_{DM}$ vs. in-situ fraction $f_{in-situ}$ for the Magneticum galaxies, with colors indicating the different accretion classes.

dark-matter fractions than ETGs. This can also be seen in the left panel of Figure 9 where we included the observational results for LTGs and ETGs from Tortora et al. (2019) and Tortora et al. (2014), respectively. As can immediately be seen, most of the class D and F galaxies clearly resemble the properties of the LTGs, while the clear observed correlation between $f_{DM}$ and $M_*$ for ETGs is most strongly populated by galaxies of the classical accretion profile class C, in good agreement with the idea that dry merging lowers the central dark-matter fractions while wet merging and smooth gas accretion lead to larger central dark-matter fractions. This correlation between the central dark-matter fractions and the stellar masses of ETGS and its evolution with redshift, including fits to the evolution trends driven by the mergers, has already been studied in detail by Remus et al. (2017). However, the details of the interactions between the baryons and the dark matter in the centers of galaxies and the influence of gas and feedback on this interaction are currently under debate and are beyond the scope of this work.

### 3.5. Accreted Mass Fractions and Transition Radii

As discussed before, for most galaxies there exists a radius at which the contribution from in-situ and accreted stars is 50% each, that is at which the dominance of the two components switches. We call this radius the *transition radius* $r_{trans}$. For our classic profile (class C), this is the radius where the dominant stellar component switches from in situ in the center to accreted in the outskirts, and thus separates the inner, self-made part of the galaxy from the outer, dry-merger dominated part.

Previous works by Cooper et al. (2013) and Rodriguez-Gomez et al. (2016) already reported this radius to be smaller for larger stellar masses and smaller in-situ fractions, and we confirm these general trends for our class C galaxies as shown in Figure 10. However, we do not find a tight correlation between the transition radius and stellar mass, and only a weak correlation is seen between transition radius and in-situ fraction (see upper panels of Figure 10), with a large scatter. Only when moving to a normalized transition radius (i.e., the transition radius divided by the half-mass–radius) do the trends become more clear: we even see a clear positive correlation between normalized transition radius and in-situ fraction, very similar to the correlation found by Rodriguez-Gomez et al. (2016) but slightly less steep (see lower panels of Figure 10). We also find a clear negative trend between the in-situ fractions and the stellar mass, with galaxies that have accreted a lot of material (i.e., high-mass galaxies) tending to have normalized transition radii of $r_{trans}/r_{1/2} \leqslant 1$. However, this trend is more of an upper limit for the in-situ fractions at a given mass, as we also find low-mass galaxies with normalized transition radii $r_{trans}/r_{1/2} \leqslant 1$, but basically no high-mass galaxies with $r_{trans}/r_{1/2} > 1$. The trend found for the Magneticum galaxies is weaker than what has been found by Rodriguez-Gomez et al. (2016) and much weaker than the trend reported for the IllustrisTNG ETGs by Pulsoni et al. (2021).[6] This reflects the fact that galaxies in Magneticum have, on average, accreted more dry stellar mass through mergers than galaxies from Illustris or IllustrisTNG.

So far, we only discussed those galaxies of profile class C as most previous works only discussed this profile class with no mention of other profile classes. For classes A and F, we cannot provide a transition radius as these galaxies are always dominated by accreted or in-situ stars, respectively, but for the profile classes B, D, and E such transition radii exist: Galaxies of class B usually have a very small transition radius of only about 2 kpc, close to the limits of our spatial resolution (and hence may be somewhat smaller than indicated). We do not find any trend, positive or negative, with stellar mass, and

[6] We note that Pulsoni et al. (2021) only show the transition radius for their centrally fast rotators of profile class 2 (equivalent to our classic profile) as a function of "effective radius" (their edge-on projected half-mass–radius).

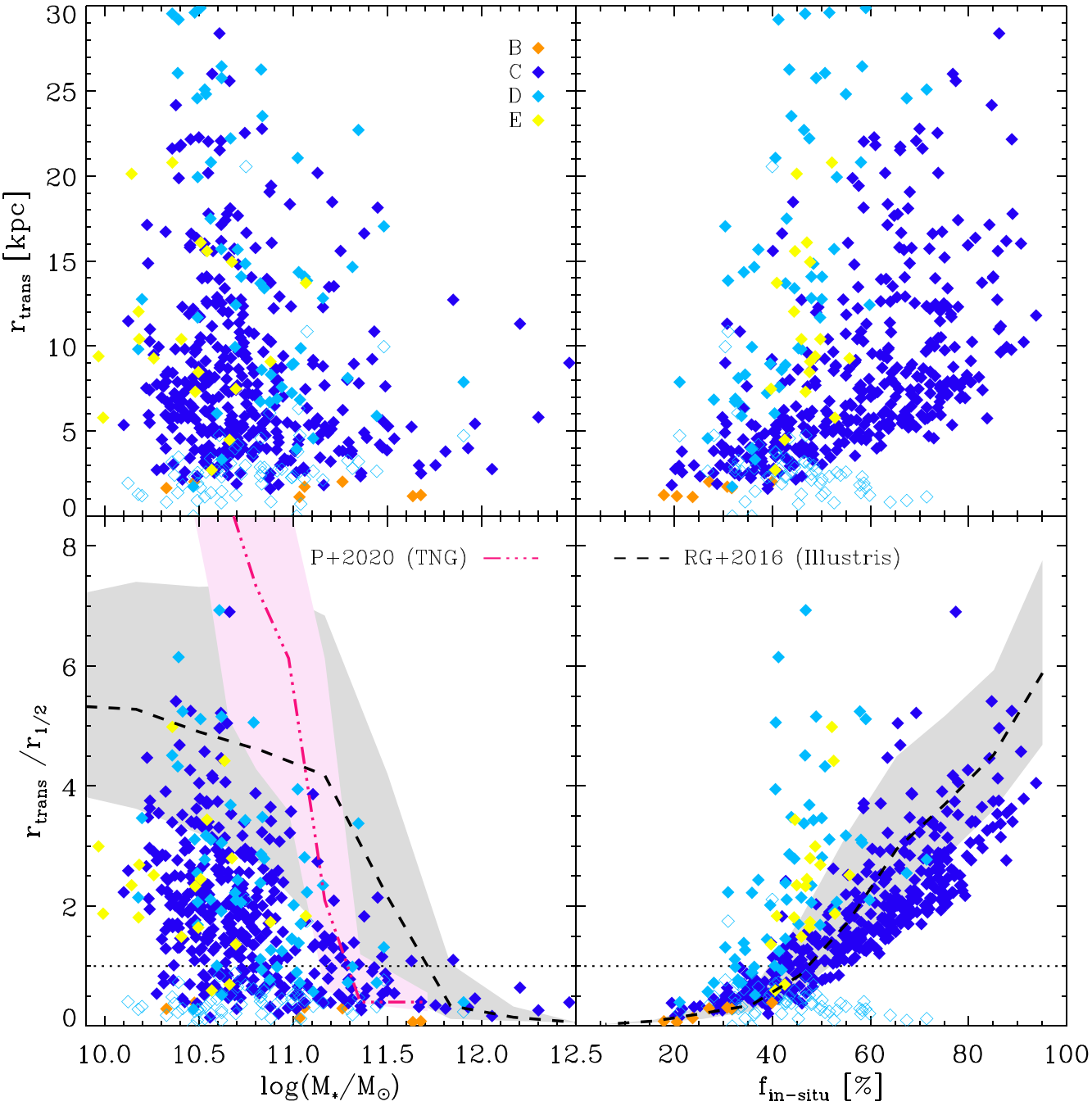


**Figure 10.** Transition radius trends for all profile classes as indicated in the label. Classes A and F have no transition radii and are therefore not shown. Class D galaxies (cyan diamonds) have two transition radii, so the outer ones are shown as filled diamonds and the inner ones are shown as open diamonds. Upper left panel: stellar mass $M_*$ vs. 3D transition radius $r_{\rm trans}$ in kpc. Upper right panel: in-situ fraction $f_{\rm in-situ}$ vs. transition radius $r_{\rm trans}$ in kpc. Lower left panel: stellar mass $M_*$ vs. 3D transition radius $r_{\rm trans}$ normalized by 3D half-mass–radius $r_{1/2}$. Lower right panel: in-situ fraction $f_{\rm in-situ}$ vs. normalized transition radius. The horizontal line in both lower panels represents a normalized transition radius of 1 half-mass–radius, i.e., $r_{\rm trans}/r_{1/2} = 1$. Dashed black lines and shaded areas show the results from the Illustris simulation (Rodriguez-Gomez et al. 2016), and the dashed–dotted–dot–dotted pink line and shaded area are the results found for ETGs only in IllustrisTNG (Pulsoni et al. 2021). The horizontal dotted line marks where the transition radius equals the half-mass–radius.

only a weak positive correlation between in-situ fraction and normalized transition radius. This is not surprising as this class is very close to being overmerged like class A, and thus we do not expect the transition radius to have any relevant meaning.

In the case of class D, where the center and the outskirts are dominated by accreted stars but the middle radial range is dominated by in-situ stars, even two transition radii exist. For the outer transition radii of class D (filled cyan symbols in Figure 10) and class E, we find the trend with in-situ fraction to be very similar, but generally steeper than the correlation seen for class C. This is even clearer for the normalized transition radii again. For both classes we also find a tighter anticorrelation between normalized transition radius and stellar mass, although the scatter is still large.

The inner transition radii for class D galaxies (open cyan diamonds in Figure 10) are usually comparably small and often well below the half-mass–radius. Generally, the inner transition radii of class D behave significantly different from all other

transition radii, as there is no trend at all for the stellar mass, neither with the transition radius nor with the normalized transition radius, and there is actually a negative trend with in-situ fraction, clearly showing that the larger the fraction of stars formed in situ, the smaller the accreted core in the center, indicating that more stars are formed in situ if the mass accreted onto the center was small compared to the gas disk of the progenitor galaxy.

As these transition radii are very indicative of the accretion history of the galaxies and may provide a method to estimate the in-situ fraction of a galaxy, it would be very instructive to be able to measure this transition radius observationally. Therefore, in Section 4 we address the question of whether it is possible to measure the radius of the transition from in-situ to accretion dominance from the observed surface brightness profiles of galaxies, as suggested by Cooper et al. (2013) and Rodriguez-Gomez et al. (2016).

## 4. Accreted Fractions from Sérsic Fits for Simulated Galaxies

Motivated by previous simulation results from Cooper et al. (2013) and Rodriguez-Gomez et al. (2016), there have been observational attempts to measure the in-situ and accreted fractions of galaxies using a double Sérsic fit (Sérsic 1963) to the observed surface brightness profiles of galaxies. This assumes that the inner Sérsic fit describes the in-situ component of the galaxy, and the outer Sérsic fit describes the accreted component. In some cases, a third fit to the very outskirts of a galaxy was carried out, under the assumption that the third component describes the stellar halo of the galaxy and not the galaxy itself (e.g., Spavone et al. 2017), but we will not investigate this approach here. Instead, we investigate in this section from our simulated galaxies if the double Sérsic approach really supplies a good measure for the in-situ and accreted components of galaxies.

### 4.1. Sérsic Fits to Projected Surface Density Profiles of Simulated Galaxies

To compare the simulated mass density profiles with observed surface brightness profiles, we need to create 2D projections of the simulated galaxies. As this projection is rather arbitrary, we choose a random projection along with the face-on and edge-on projections to test for each galaxy in our sample. In all cases, we find that the profile class of our galaxies does not change, and the in-situ to accreted relations stay the same under all projections. Thus, for all galaxies that have a transition radius ($r_{\rm trans}$) in 3D, we also find a radius in the 2D projections which indicates a transition from in-situ to accretion dominance.

Observationally, fits are made to surface brightness profiles and light-weighted radii are measured. Our simulations produce 2D mass surface density profiles in units of $M_{\odot}/{\rm kpc}^2$. In order to make a direct comparison one requires radial stellar mass-to-light ($M/L$) profiles. However, Zheng et al. (2015) have shown that high-mass galaxies with stellar mass $\log(M_*) > 10.5$ (i.e., comparable to our lower limit) have relatively constant $M/L$ profiles with radius, and thus light and 2D mass density profiles are similar on average. Individual galaxies may of course have strong radially variable $M/L$ profiles. With this caveat in mind, we fit our projected mass density profiles with both single and double Sérsic fits. For profile fits, in both 2D and 3D, we exclude the innermost kpc in the fit as this is below the softening limit and thus the profiles always become artificially flat in the inner parts. Similarly, the inner regions of observed galaxies are often not fit due to seeing effects.

In most cases, a double Sérsic fit is a better fit to the projected mass profiles, independent of the projection. In those cases where a single Sérsic fit is sufficient, this is true for all tested projections. This is rather promising as it clearly indicates that, if a double Sérsic fit is needed to describe the observed surface brightness profile, then it is independent of the viewing angle and reflects the underlying 3D density distribution. For the double Sérsic fits to the 2D mass density profiles, we define the crossing radius, $R_{\rm cross}$, as the radius where the inner and outer Sérsic profiles cross each other.

In Figure 11 we show examples of our profiles in 3D and in each projection. The upper row of Figure 11 shows an example of a class C profile galaxy with its well-defined transition radius in 3D (here $r_{\rm trans} = 10.52$ kpc, left panel). A transition is also seen between the in-situ and accretion-dominated regions of the galaxy in all three 2D projections (upper right panels); however, the values of the transition radii in the 2D projections are all smaller than the 3D transition radius $r_{\rm trans}$. We find that this is not simply a matter of unlucky projections but is rather a common feature of class C profiles (which make up the majority of profiles). This disconnect between the transition radii seen in 3D and the 2D profiles also occurs in all other classes with well-defined transition radii, namely classes B, D, and E.

While the transition radii are already disconnected from 3D to 2D, the matter is even worse if we use the double Sérsic fits to describe the underlying in-situ and accreted components: In a few cases like the one shown in the upper panels of Figure 11, the two Sérsic components are a good approximation of the in-situ and accreted components, and the resulting crossing radius between the two Sérsic components, $R_{\rm cross}$, is a good approximation to the 2D transition radius. However, for most galaxies this is not the case. One example of a galaxy that demonstrates the issue nicely is shown in the lower panels of Figure 11: This galaxy is of class A, i.e., is accretion dominated at all radii and has no transition radius from in-situ to accretion dominated, neither in 3D (left lower panel) nor in projection (three panels on the lower right). However, the stellar 2D surface density profiles in this example, under all projections, clearly require a double Sérsic fit, thus providing a crossing radius $R_{\rm cross}$. The two resulting Sérsic components in this case do not describe the underlying in-situ and accreted components. They instead mark the radius where accretion due to massive mergers transitions into accretion from small mergers and mini mergers that never reach the center of the galaxy. We note that in the case of class C galaxies, which possess clear in-situ and accreted components, usually both can individually be fit well by a Sérsic profile, even though they cannot be recovered from the double Sérsic fits.

To further quantify this issue, the left panel of Figure 12 shows the differences between the crossing radii of the double Sérsic fits $R_{\rm cross}$ for the random projection (with error bars marking the values for the edge-on and face-on projections), and the true 3D transition radius $r_{\rm trans}$ between the in-situ and accreted components for all galaxies where such a transition radius is well defined (classes B, C, D, and E). The plot is largely a scatter diagram with little, or no, correspondence between the two measured radii, independent of the profile class. This is also

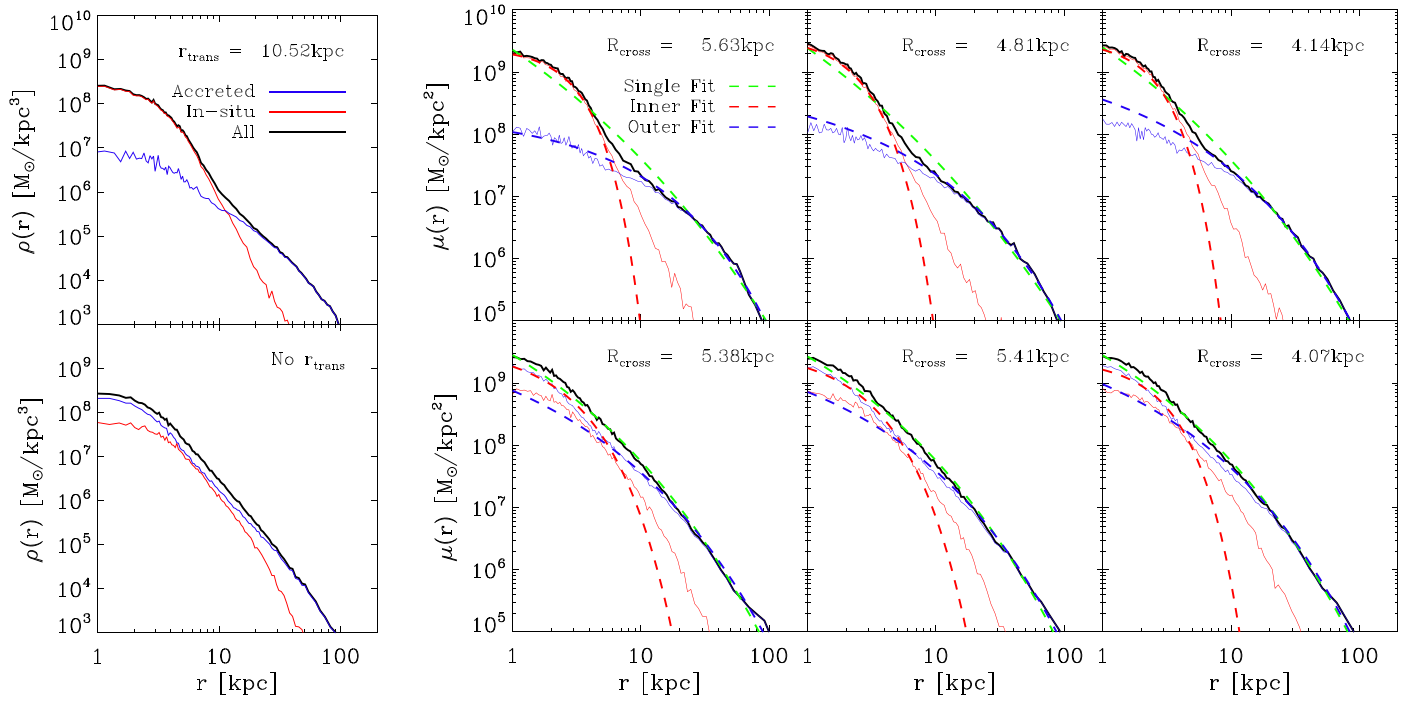


**Figure 11.** Upper panels: example of a class C mass density profile in 3D and 2D projections. Top left panel: 3D total stellar mass density profile (black curve) with the in-situ and accreted components in red and blue, respectively. Top right panels: projected 2D stellar mass density profiles from three different projections: The projected total stellar profile is shown as a black curve, and the in-situ and accreted components are shown as solid red and blue lines, respectively. The dashed lines show the inner (red) and the outer (blue) fits from the double Sérsic fits, and the single Sérsic fits (green) to the total projected stellar density profiles. In the upper right of each panel we list the transition radius in 3D and the crossing radii in 2D, in units of kpc. In this example, the single Sérsic fit is never a good fit for any of the projections. The double Sérsic fits describe the total profile very well in all projections, and are also a good approximation to the in-situ and accreted profiles in all cases. However, the crossing radii $R_{\rm cross}$ (i.e., the radius where the two Sérsic profiles cross) vary on the order of 1 kpc between the three projections, and are in all three cases only about half as large as the real 3D transition radius $r_{\rm trans}$. Lower panels: same as upper panels but for a class A profile. Class A galaxies are extremely accretion dominated and have no transition radius between in-situ and accreted components in their 3D or 2D stellar density profiles, as can be seen from the solid red and blue curves in all four panels. However, a single Sérsic fit is not a good fit to any of the projections and the double Sérsic fit is clearly needed in all three projections to describe the total total stellar profiles. Thus, we obtain crossing radii $R_{\rm cross}$ from these double Sérsic components that vary again between the three projections, but in no case are they representative of the true in-situ or accreted components.

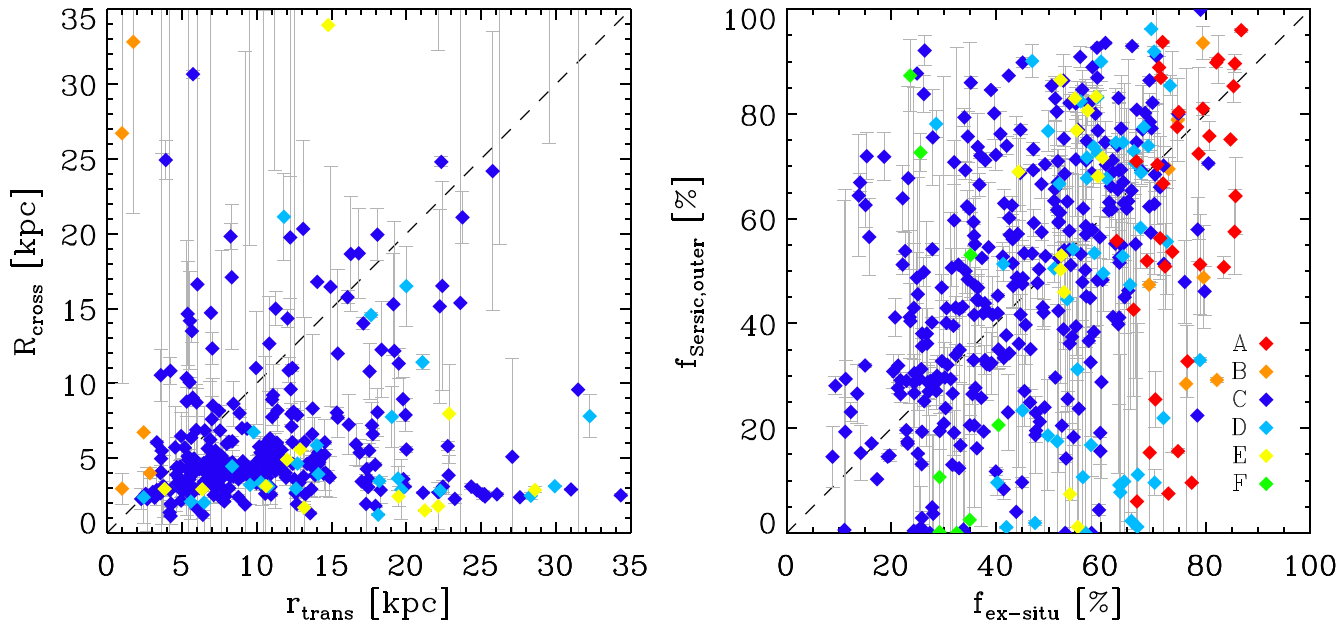


**Figure 12.** Double Sérsic fits to Magneticum galaxies. Left panel: crossing radius $R_{\rm cross}$ obtained from double Sérsic fits to the 2D projected mass density profiles (random projection) vs. the 3D transition radius $r_{\rm trans}$ between in-situ and accreted components, for all profile classes (colors as indicated in the right panel) with well-defined transition radii. Right panel: fraction of integrated mass from the outer Sérsic function fit to the 2D mass density profiles vs. the true accreted mass fraction. In both panels, the dashed line shows a 1:1 relation. Error bars indicate the maximum and minimum values obtained for edge-on and face-on projections.

true for the projected 2D transition radii, but as the behavior is nearly identical we do not show this plot here.

For galaxies of classes D and E, the 2D crossing radii are much smaller than the real transition radii, while for galaxies of class B we find the opposite trend (with two of them having such large crossing radii $R_{\rm cross}$ that they are well above the plotted radius range). Galaxies of class C show both kinds of behavior, with $R_{\rm cross}$ both lower and higher than the true $r_{\rm trans}$. Independent of the profile class, we conclude that it is a lucky coincidence if the crossing radius $R_{\rm cross}$ of the double Sérsic fits is a good approximation to the transition radius $r_{\rm trans}$. In summary, the transition from an inner to an outer Sérsic fit to an observed surface brightness profile bears little, or no, connection to the true transition between the in-situ and accreted components in a galaxy.

We also measure the integrated mass within the outer Sérsic component and compare it to the true accreted mass fraction. This is shown in the right panel of Figure 12 for all galaxies where a double Sérsic fit was a good fit, even those of profile classes A and E that are dominated by accreted or in-situ stars at all radii, respectively, and thus do not have a transition radius. This plot reveals a large scatter with a very weak trend about the unity line, indicating that an outer (inner) Sérsic component fit to a surface brightness profile is a poor guide to the true accreted (in-situ) mass fraction.

In summary, we find that fitting a double Sérsic profile to the 2D surface density profile of model galaxies does not reveal the true radius for the transition from in-situ to accretion-dominated material. This suggests that the dips seen in observed surface brightness profiles of ETGs cannot, in general, be taken as a signature of a division between in-situ and accreted components of the galaxy. They may instead be more indicative of a transition from stars being formed in-situ plus stars accreted by major mergers, to the component of stars mostly accreted through minor or mini mergers. Furthermore, the integrated mass associated with the inner and outer Sérsic functions provide a poor guide to the true in-situ and accreted mass fractions of a galaxy, respectively.

In this work we have fit 1D profiles, as is often the approach for observations of galaxies (i.e., fits to surface brightness profiles). However, galaxies can also be fit in 2D from imaging. Such an approach can include the effects of changes in position angle, ellipticity, boxy/diskyness, asymmetries, etc. in the isophotes. Indeed, Magneticum model galaxies also reveal "isophotal" changes with radius and become less symmetric at larger radii (L. M. Valenzuela et al. 2022, in preparation). Our initial tests suggest radial changes have little impact on our conclusions, but this warrants detailed investigation in a future study.

We conclude that the (two) components visible in the (projected) density profiles do not reflect the in-situ and accreted components in general, but rather mark the transition from the inner part of the galaxy which can be dominated by in-situ stars but can also be dominated by a massive merger event, and the outer part of the galaxy which is dominated by small minor or mini mergers that get disrupted in the outskirts of the galaxy and never interact with its center.[7] This is similar to the dynamical split of the ICL and the BCG in galaxy clusters, and might be a way to distinguish outer stellar halos of galaxies from the galaxies themselves instead.

[7] Note that in the very inner parts of galaxies additional components can be visible in the (projected) density profiles, caused for example by bars and bulges, but we cannot include these structures in our analysis as the resolution of the Magneticum galaxies is not high enough to resolve these inner structures of the galaxies.

## 5. Comparison with Observations

Some of the deepest imaging of nearby galaxies available comes from the VEGAS survey of ETGs (Capaccioli et al. 2015). The survey probes surface brightness profiles out to $\sim$10 $R_{\rm e}$ and down to surface brightness levels of $\sim$29 mag/ arcsec$^2$ in the $g$-band. The survey is still ongoing, however, results on the radial surface brightness profiles have been published for several massive galaxies in group/cluster environments by Spavone et al. (2017) and Spavone et al. (2020). Spavone et al. (2017) fit two or three Sérsic profiles to six ETGs, with the Sérsic parameters $n$ constrained to a narrow range. More recently, Spavone et al. (2020) fit 19 ETGs in the Fornax cluster with either two or three Sérsic components. Here we focus on the two-component fit, for which $n$ was a free parameter. The two-component fits have a single intermediate radius, and the accreted mass fractions are calculated from the second (outer) component. These are referred to as the "relaxed" components following Cooper et al. (2015). Hence the approach to providing unconstrained fits is more comparable to our approach, we focus on the study by Spavone et al. (2020) instead of Spavone et al. (2017).

Another very deep imaging study has been carried out by Kluge et al. (2020), who fit double Sérsic profiles to extremely low surface brightness profiles targeting especially BCGs. Both single and double Sérsic fits were obtained, as well as accreted fractions from the double Sérsic fits. For the VEGAS survey, several of their ETGs are of similar stellar mass to the mass range probed in this study. However, our simulated sample only includes a handful of BCGs due to the small box size, and thus a statistical comparison to the BCG sample of Kluge et al. (2020) is not possible here. Nevertheless, general trends can still be analyzed.

We also compare to the double Sérsic fits of $\sim$45,500 galaxies, observed at a mean redshift $z \sim 0.08$ and stacked in mass bins by D'Souza et al. (2014). Taking mean values from their Figure 13 for ETG-like galaxies, we note that their data covers a similar stellar mass range to our modeled galaxies and that they find effective radii of the inner and outer components to be around 3 and 8 kpc, respectively.

### 5.1. Accreted Fractions from Double Sérsic Fits

Figure 13 shows the ex-situ accretion fraction versus stellar mass. The solid and dashed blue lines show the average fraction of accreted mass for all Magneticum galaxies, for the true ex-situ fraction (dashed line, as in Figure 6), and the mass fraction obtained from the outer Sérsic fits (solid line), resembling the observationally used proxy for the ex-situ fraction. In addition, we included the ex-situ fractions inferred from the outer Sérsic fit in a random projection for our simulated ETGs as little diamonds, color coded again according to their accretion class. The correlation of the Sérsic-inferred ex-situ fractions with mass is much weaker than the real underlying correlation between the mass and the real ex-situ fraction, and the scatter is huge as can clearly be seen from the points of the individual ETGs. Especially at the higher masses, the average Sérsic-inferred ex-situ fractions are much lower on average than the true average ex-situ fractions, reflecting the huge scatter in individual data points.

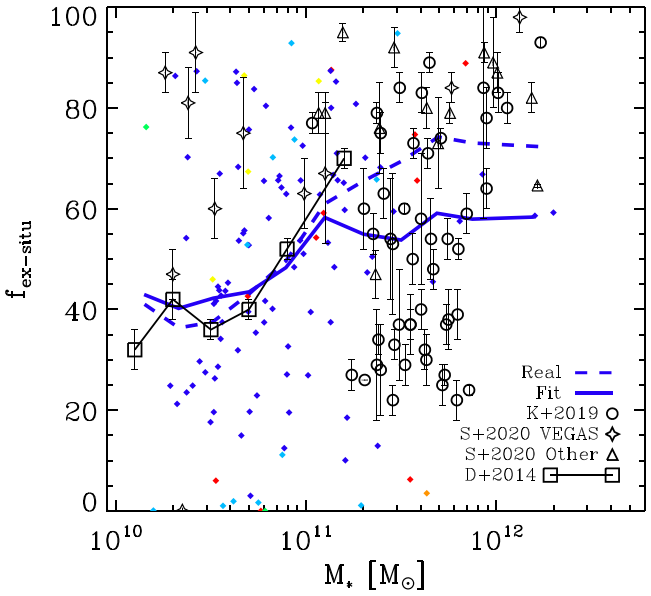


**Figure 13.** Mass fraction of accreted stars vs. stellar mass for ETGs. Observational data points from the VEGAS survey of Spavone et al. (2020) are shown as open diamonds, with additional data points from the literature as presented by Spavone et al. (2020) as open triangles. Data points for BCGs from Kluge et al. (2020) are shown as filled black diamonds. The values for stacked ETGs from D'Souza et al. (2014) are shown as open squares. The blue solid line indicates the mass associated with the fit to the outer Sérsic component for all Magneticum galaxies for which a double fit could be obtained. The blue dashed line shows the true accreted mass fraction for Magneticum galaxies (as shown in Figure 6). The small colored symbols represent the outer Sérsic fit mass fractions for individual Magneticum ETGs (color coded according to their accretion class as in Figure 6).

We also include in Figure 13 various observational data of ETGs from Spavone et al. (2020), Kluge et al. (2020), and D'Souza et al. (2014). These observations infer the fraction of accreted mass through double Sérsic fits to the surface brightness, as described above, using the mass fraction from the outer Sérsic component by assuming a stellar $M/L$ ratio of 1.

While simulations generally find a trend of increasing ex-situ fraction for higher galaxy masses, there is no clear trend for the observational proxy (the outer component mass) to vary with stellar mass, neither for the Fornax cluster galaxies of Spavone et al. (2020), nor the BCG sample of Kluge et al. (2020). Only the stacked sample provided by D'Souza et al. (2014) shows an increase in accreted fraction with stellar mass for their ETG sample. It also nicely matches the mean trend for all galaxies in Magneticum over the common mass range. (We note that LTGs make up only ∼20% of all galaxies.) Overall, however, the different observations differ strongly from each other and do not show a clear picture of the accreted mass fraction, estimated via the outer Sérsic fit component, being correlated with the total stellar mass of a galaxy. In this regard, the observations resemble the Sérsic-derived values from the simulations, showing no visible trend with mass, in contrast to the actual real ex-situ fractions. This further supports our results from Section 4.1, that the outer Sérsic fit, in general, does not correspond to the true transition from in-situ to accreted dominated material and thus is not a good proxy for the true ex-situ fraction of galaxies. An alternative approach to estimating accretion fraction may come from star formation histories (Boecker et al. 2020) or 2D chemodynamical analysis (Poci et al. 2019), and this needs to be investigated further in future studies.

### 5.2. Radial Density Profile Shapes Between Observations and Simulations

So far, we have compared the global properties inferred from double Sérsic fits to simulations and observations. While we have seen that the simulated galaxies successfully reproduce the observed sizes and stellar masses, it is also important that the actual shapes of the radial surface density profiles match the surface brightness profiles obtained from observations. To highlight this, we focus on directly comparing three example radial surface brightness profiles from observations to three radial surface density profiles from the Magneticum sample, matched in their stellar mass. We use an M/L ratio of 1 here, assuming it to be radially constant which is a reasonable assumption as discussed above. Given that the M/L ratio can have different values for different galaxies, changes in normalization in the relative density can easily be achieved by changing M/L for a given galaxy. Consequently, this comparison focuses on the shape of the radial profile and the Sérsic indices obtained from fits over the same radial range which are independent of such scaling factors.

We chose three observed galaxies with very different radial profiles: A BCG in A1400 from Kluge et al. (2020) and two ETGs from Ragusa et al. (2022) from the VEGAS survey, i.e., NGC 3379 and NGC 2284. Figure 14 shows the resulting comparison, with the simulated profiles and the corresponding single and double Sérsic fits in red and the observed profiles and their Sérsic fits in black. As can clearly be seen, all three radial surface brightness profiles can be reproduced by galaxies of similar mass from the Magneticum simulation. This shows that a comparison between simulations and observations can be performed as the radial mass profiles of the Magneticum simulations mirror those of observed galaxies. The Sérsic indices for the fits to the observed and simulated galaxies are listed in Table 2, indicating that the Sérsic n values are very similar as well.

Note that the fits to the observed profiles are not the same as those performed by Kluge et al. (2020) and Ragusa et al. (2022), since different radial ranges were used, especially for NGC 3384, where the radial profile reaches further in than the resolution limit of our simulation. Thus, NCG 3384 needs a double Sérsic fit to the full radial profile, while here we focus on the outer radii. We find that for both the simulated and the observed profiles a single Sérsic fit is sufficient. The mass density offset seen for the BCG of A1400 and the Magneticum BCG vanishes if $M/L = 3$ is used.

We remind the reader that the limitations in the radial range that can be probed due to the softening length in the simulations needs to be considered, and thus the very central parts cannot be fit. Higher resolution simulations in the future will be needed to discern the nature of these very inner components. However, to study the outskirts and the radial ranges where the in-situ and accreted fractions change dominance, the simulations used here are more than sufficient.

### 5.3. Sérsic Indices from Single and Double Fits

As a final test, we compare the Sérsic indices $n$ from the single and double Sérsic fits to our projected simulated galaxies with observations to ensure that the simulated and observed

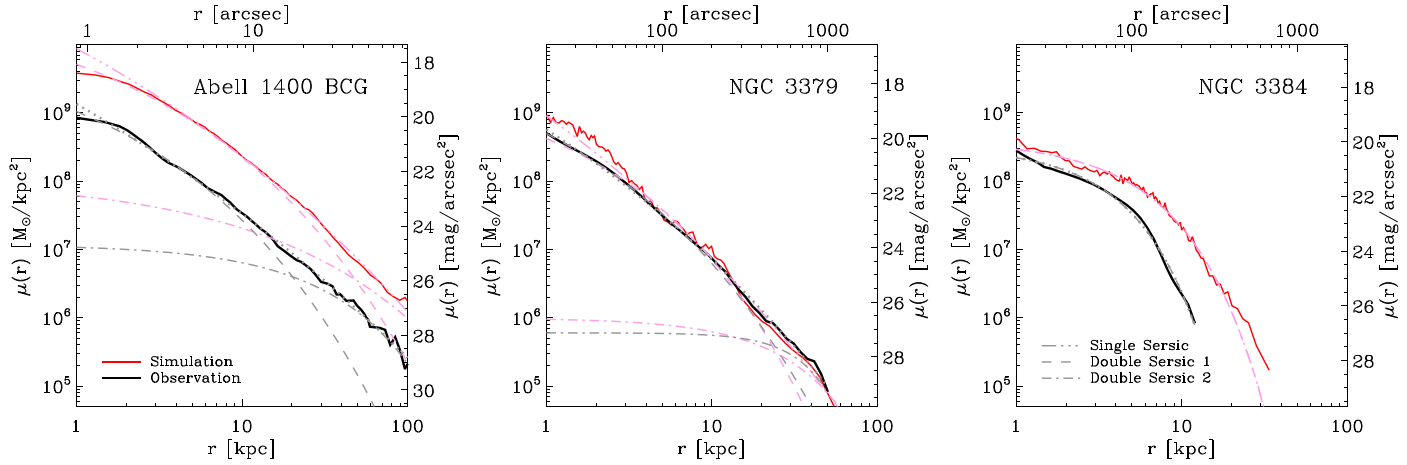


**Figure 14.** Example radial surface density profiles for three Magneticum galaxies (red curves) selected to match in stellar mass with three observed galaxies (black curves). Left panel: the BCG of the galaxy cluster A1400 taken from Kluge et al. (2020); Middle panel: NGC 3379 in the Leo Group from the VEGAS survey, profile published by Ragusa et al. (2022); Right panel: NGC 3384 in the Leo Group from the VEGAS survey, profile published by Ragusa et al. (2022). Here, the central parts of the galaxies are excluded both for observations and simulations, as the resolution limit of the simulation does not allow for properly probing the radial range below 1 kpc. Dashed lines indicate results from single and double Sérsic fits to both the observed and simulated profiles. The Sérsic indices found for these fits are listed in Table 2. In this comparison an M/L ratio of 1 is used, thus the profiles can be shifted up and down in mass density using different M/L.

**Table 2**
Sérsic Indices of the Fits to the Observed and Simulated Galaxy Radial Surface Density Profiles

| Name | $n_{\rm Single}$ | $n_{\rm 1,Double}$ | $n_{\rm 2,Double}$ |
|---|---|---|---|
| A1400 | 8.54 | 2.67 | 1.22 |
| Magneticum 6 | 6.31 | 2.91 | 2.26 |
| NGC 3379 | 5.92 | 2.97 | 0.50 |
| Magneticum 543 | 6.38 | 2.21 | 0.94 |
| NGC 3384 | 0.89 | 0.89 | … |
| Magneticum 576 | 1.02 | 1.02 | … |

**Note.** The observed profiles are taken from Kluge et al. (2020) for the BCG of the galaxy cluster A1400 and from Ragusa et al. (2022) for NGC 3379 and NGC 3384. The Sérsic fits are not taken from these papers, however, but are fitted with the same routine used to fit the simulated data to ensure the same radial range is covered and the methods are identical. In the case of NGC 3384, a single Sérsic fit was sufficient to describe the profile even when trying to fit double Sérsic profiles, hence there is no second Sérsic index, and the first Sérsic index is identical to the single Sérsic fit index.

galaxy samples really are comparable in their radial properties. Figure 15 shows the Sérsic indices $n$ from single Sérsic fits to the 2D projected mass density profiles of the Magneticum galaxies, for all galaxies in the left panel and ETGs only in the right panel. We find a trend of increasing Sérsic index $n$ for higher-mass galaxies. Galaxies of the different profile classes are well spread in the Sérsic index for a given stellar mass, with no clear trends apart from the fact that the largest Sérsic indices are clearly found in class C galaxies.

When limiting our galaxy sample to ETGs only (right panel of Figure 15), we find the Sérsic indices to be slightly larger on average. We additionally include the observational data for individual ETGs from Kormendy et al. (2009) and Kluge et al. (2020) and the mean relation for ETGs using Equation (2.7) from Graham (2013) while simply assuming $M/L_{\rm B} = 10$. We find a generally good agreement between the Sérsic indices found for our simulated ETGs and the observations. This shows that the simulations also provide good descriptions of the stellar mass distributions in ETGs especially. There is a slight tendency for galaxies with stellar masses above $\log(M_*) > 11.5$ to have larger Sérsic indices in the observed samples than in our simulated sample, however, at this mass range our simulated sample is statistically not representative anymore, especially since there are only four BCGs in our sample while the observations by Kluge et al. (2020) are of BCGs only.

For double Sérsic fits, we focus only on ETGs. As shown in Figure 16, we find the inner profiles of our simulated ETGs to have Sérsic indices of $n \sim 2.5$ on average (left panel), and the outer profiles to have Sérsic indices of $n \sim 0.5$–1, on average (right panel). We find little variation of these indices with stellar mass, if all there is a slight average trend for the inner Sérsic indices of more massive galaxies to be slightly larger. The agreement with the nine ETGs from the VEGAS survey (Spavone et al. 2020), with masses $> 10^{10}\ M_{\odot}$, is reasonable, with a slight tendency for the observed outer Sérsic indices to be larger than for the simulated ETGs. Compared to the observations of BCGs by Kluge et al. (2020), we find that the agreement with their outer Sérsic indices is rather good, while their inner Sérsic values are on average larger than those of our simulated galaxies. However, this could also be due to the fact that most of the Magneticum ETGs in the mass range comparable to the sample by Kluge et al. (2020) are not BCGs.

Additionally, we also show in Figure 16 the inner and outer Sérsic indices from the stacked observations by D'Souza et al. (2014), using their double Sérsic fits (solid lines). As can clearly be seen they differ rather strongly from the simulated galaxies, but also from the other observations, with their inner slopes generally smaller and their outer slopes much larger. We note that D'Souza et al. (2014) also fit triple Sérsic profiles to their highest mass galaxies. In this case, their outer Sérsic fits have $n \sim 1.5$, which is much closer to our simulation values and the other observations, indicating that their inner slopes are actually really "inner" slopes which we do not fit in this work to avoid resolution issues. This clearly highlights the importance of clear definitions regarding the fitted regions of galaxies when performing comparisons.

Overall, we find reasonable agreement between the Sérsic indices $n$ predicted by our simulated galaxies and the observed

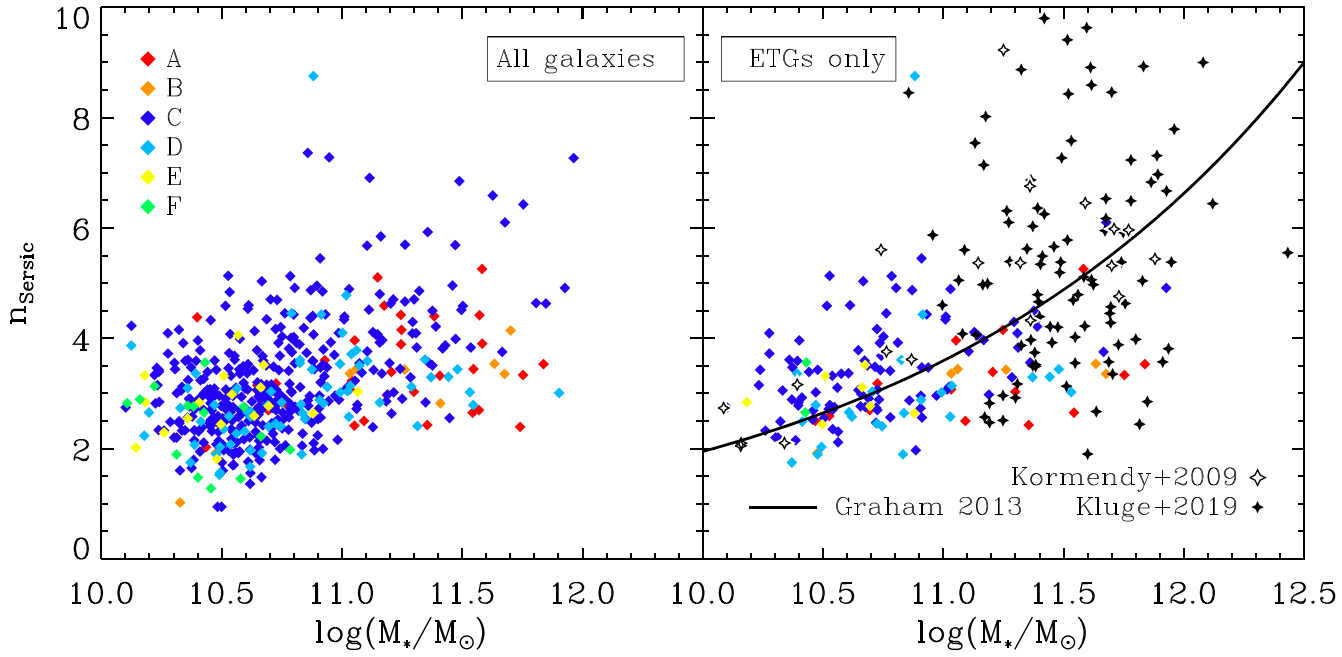


**Figure 15.** Sérsic index $n$ vs. stellar mass for single Sérsic fits to the 2D projected mass density profiles of Magneticum galaxies. Left panel: all Magneticum galaxies are colored according to their profile classes as indicated in the legend. Right panel: only the ETGs from the Magneticum galaxy sample are shown. In addition, open black diamonds show observations of ETGs from Kormendy et al. (2009), and the solid black diamonds show BCGs from the observations by Kluge et al. (2020). The solid black line is the mean relation from observations by Graham (2013) converted into stellar mass assuming $M/L_B = 10$.

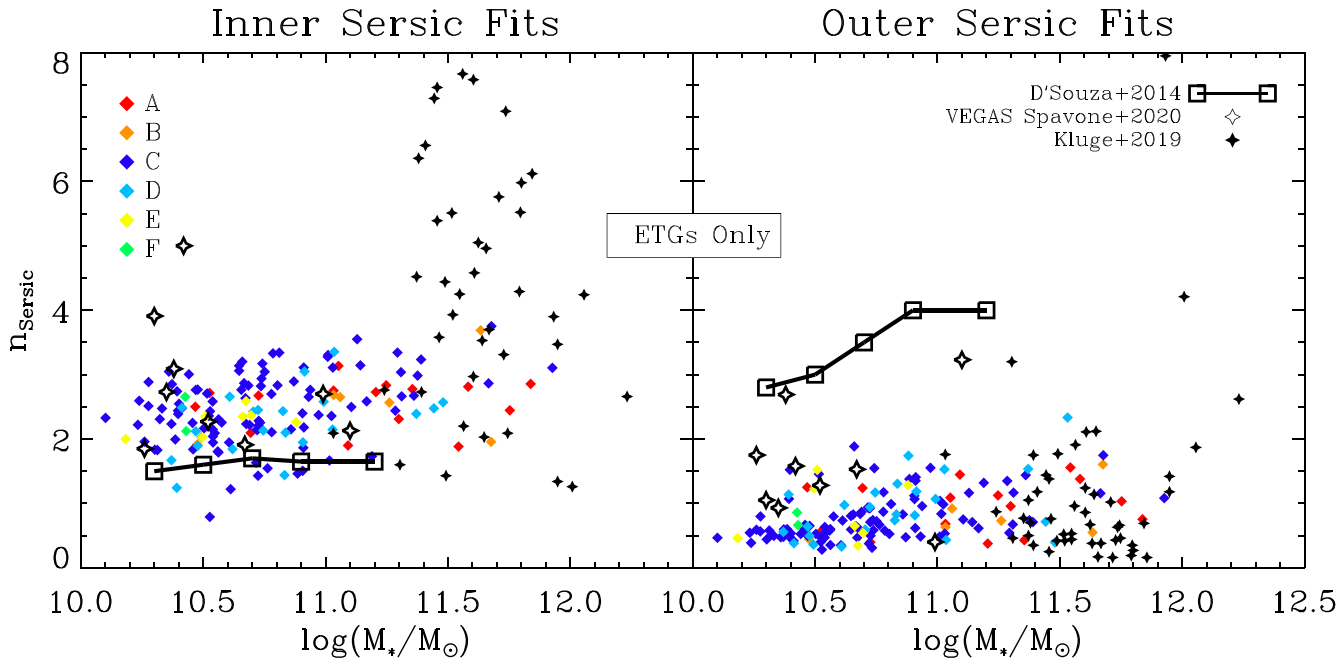


**Figure 16.** Sérsic index $n$ vs. stellar mass for double Sérsic fits to the 2D projected mass density profiles of the Magneticum ETGs, with colors as indicated in the legend. Observations from the VEGAS survey (Spavone et al. 2020) are shown as open black diamonds, and BCGs from Kluge et al. (2020) as solid black diamonds. The squares and black lines indicate the stacked ETGs from D'Souza et al. (2014). Left panel: inner Sérsic fits. Right panel: outer Sérsic fits.

Sérsic indices, for both single and double Sérsic fit indices, clearly showing that the simulated galaxies used in this work capture the observed matter distributions. This indicates that our result, that double Sérsic fits do not accurately describe the in-situ and accreted components of galaxies, is also applicable to observations. We rather suggest that the double Sérsic fit (excluding the central inner bulge areas) describes the relaxed inner and the unrelaxed outer stellar (halo) components of galaxies and could therefore be used to distinguish the outer stellar halo from its galaxy.

## 6. Summary and Conclusions

Using the Magneticum simulation we have studied a sample of 511 model galaxies in the halo mass range of $11 < \log(M_{\rm tot})$, corresponding to a stellar-mass range of $10.1 < \log(M_*) < 12$.

These simulated galaxies reproduce well the observed galaxy size–mass relation. We find that the fraction of accreted material, as a function of total halo and stellar mass, reveals similar trends to those found by previous simulations, i.e., larger accretion fractions in higher-mass galaxies. One notable difference is that our simulations predict higher accretion fractions in the lower-mass galaxies than other simulations.

We examine the 3D stellar mass density profiles of our sample, split into accreted and in-situ components, and classified them into six classes depending on the profile type: The most common class reveals, at intermediate radii, a transition radius where the accreted and the in-situ component are equal, with the in-situ component being dominant in the center and the accreted component dominating the outskirts. This class is comparable to the most common profiles found in previous studies. However, for about 30% of our galaxies we find different profiles: Some are accretion dominated at all radii, even in the center; another group of galaxies is in-situ dominated at all radii; and most interestingly, we find one class of galaxies that have even two transition radii at which the in-situ and accreted material are equal, with an accretion-dominated core, an in-situ-dominated shell around it, and an accretion-dominated outskirt. This is actually the second most common class of galaxies in our sample.

We show that these profile classes correlate with galaxy mass, and that the type of mergers they undergo help shape their profiles. We especially show that the amount of gas that is involved in these mergers is more important in shaping these profiles than the actual merger, and that the most common class is not dominated by major mergers but rather smaller merger events. Their outer regions are largely built up by dry minor and mini mergers, clearly showing the importance of minor and especially mini mergers in shaping the outer stellar halos of massive galaxies.

We find that galaxies with high in-situ fractions (low accretion fractions) tend to be lower-mass galaxies with smaller half-mass radii. We also see a weak trend for high in-situ fraction galaxies to have lower central dark-matter fractions, with the exception of the overall in-situ-dominated galaxies that have clearly larger central dark-matter fractions at a given stellar mass than galaxies of the most common class, typical for what is found in disk galaxies. We measure the radius between the in-situ and accretion-dominated regions for those galaxies that reveal a clear transition, which are the majority of our sample. This transition radius is found to be weakly inversely correlated with stellar mass, but strongly correlated with the in-situ fraction for our most common class of galaxies. However, galaxies of the other classes that have one or even two transition radii do not follow the same relations.

We projected the 3D stellar mass density at different angles for each galaxy to be able to better compare our profiles with observed surface brightness profiles. We show that the radial surface density profiles of our simulated galaxies are in good agreement with the shapes of the radial surface density profiles of observed galaxies, having similar Sérsic indices overall, thus allowing a direct comparison between simulated and observed radial profiles. We find that the transition radius from in-situ to accretion-dominated profiles seen in many 3D profiles also occurs in all projections, but always at different radii in the 2D profiles, usually at smaller radii. None of our galaxies changes its in-situ profile class during projections. We also find that, similar to observations, our projected 2D stellar mass surface density profiles usually require a double Sérsic fit to be described accurately, with Sérsic indices for both components similar to the range of observed Sérsic indices. However, we clearly see that these two Sérsic components usually do not describe the underlying in-situ and accreted components, but are rather distinct from those. Only in very few cases does the crossing radius of the two Sérsic components coincide with the transition radius of the galaxy. We also clearly see that most galaxies that are dominated by accreted stars at all radii still require a double Sérsic fit to describe the 2D stellar surface density profiles, thus having a crossing radius but no true transition radius.

In other words, we conclude that the dip seen in 2D profiles does not correspond to the true transition radius between in-situ and accretion-dominated regions. Similarly, any mass inferred from these double Sérsic fits will not trace the true in-situ or accreted mass of a galaxy. Thus, fits the dips seen in some observed surface brightness profiles of ETGs are not a true measure of a galaxy's accreted material. However, they do hold some information about the assembly history of that galaxy, as we find indications that these dips are more likely an indication of the transition from the inner (in-situ and massive merger-dominated) core of a galaxy to its stellar halo (mostly accreted through minor and mini mergers), similar to the ICL component around BCGs. To confirm this, a more detailed study including also the radial kinematics of a galaxy in addition to its mass density profile is needed in the future, to disentangle the formation pathways of galaxies from observational tracers.

We thank Klaus Dolag and Felix Schulze for very useful discussions. We also thank Thomas Davison, Enrica Iodice, and Marilena Spavone for their helpful comments. We also acknowledge funding from the DAAD PPP Germany–Australia Exchange Program, project No. 57388442 . The Magneticum Pathfinder simulations were partially performed at the Leibniz-Rechenzentrum with CPU time assigned to the Project "pr86re" supported by the DFG Cluster of Excellence "Origin and Structure of the Universe." We are especially grateful for the support from M. Petkova through the Computational Center for Particle and Astrophysics (C2PAP). The data underlying this article will be shared upon reasonable request to the corresponding author.

## Appendix

As the stellar half-mass–radius of galaxies in observations is calculated from 2D projections, we also chose a random projection to calculate the half-mass–radius for each of the simulated galaxies. This allows a better comparison to the observations from Lange et al. (2015) for the GAMA survey. As can be seen in Figure 17, the Magneticum galaxies, also in projection, successfully reproduce the observed relations (shown in Figure 8).

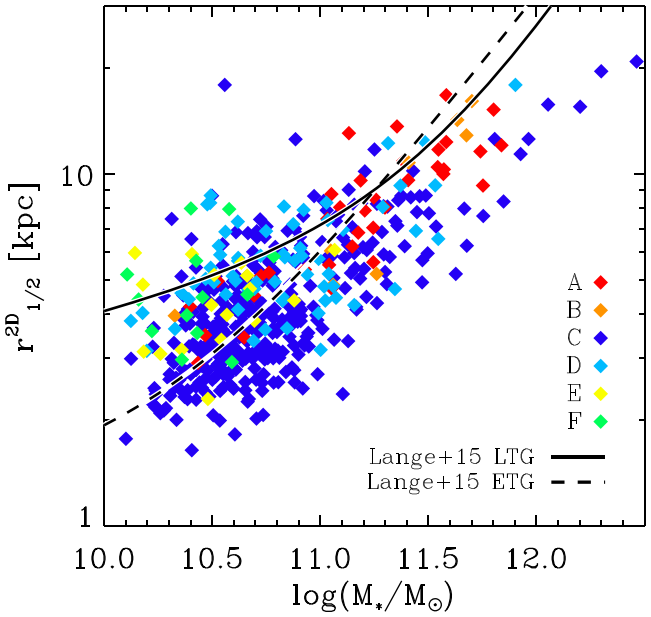


**Figure 17.** Size–stellar mass relation. Same as Figure 8 except for the half-mass–radius which is calculated for a 2D random projection.

## ORCID iDs

Duncan A. Forbes https://orcid.org/0000-0001-5590-5518

## References


Amorisco, N. C. 2017, MNRAS, 464, 2882
Beck, A. M., Murante, G., Arth, A., et al. 2016, MNRAS, 455, 2110
Biffi, V., Dolag, K., & Merloni, A. 2018, MNRAS, 481, 2213
Boecker, A., Leaman, R., van de Ven, G., et al. 2020, MNRAS, 491, 823
Capaccioli, M., Spavone, M., Grado, A., et al. 2015, A&A, 581, A10
Clauwens, B., Schaye, J., Franx, M., & Bower, R. G. 2018, MNRAS, 478, 3994
Cooper, A. P., Cole, S., Frenk, C. S., et al. 2010, MNRAS, 406, 744
Cooper, A. P., D'Souza, R., Kauffmann, G., et al. 2013, MNRAS, 434, 3348
Cooper, A. P., Gao, L., Guo, Q., et al. 2015, MNRAS, 451, 2703
Corcho-Caballero, P., Ascasibar, Y., & Scannapieco, C. 2021, MNRAS, 506, 5108
Courteau, S., & Dutton, A. A. 2015, ApJL, 801, L20
Davison, T. A., Norris, M. A., Pfeffer, J. L., Davies, J. J., & Crain, R. A. 2020, MNRAS, 497, 81
Dolag, K., Borgani, S., Murante, G., & Springel, V. 2009, MNRAS, 399, 497
Dolag, K., Jubelgas, M., Springel, V., Borgani, S., & Rasia, E. 2004, ApJL, 606, L97
Dolag, K., Mevius, E., & Remus, R.-S. 2017, Galax, 5, 35
Dolag, K., Vazza, F., Brunetti, G., & Tormen, G. 2005, MNRAS, 364, 753
Donnert, J., Dolag, K., Brunetti, G., & Cassano, R. 2013, MNRAS, 429, 3564
D'Souza, R., Kauffman, G., Wang, J., & Vegetti, S. 2014, MNRAS, 443, 1433
Dubois, Y., Gavazzi, R., Peirani, S., & Silk, J. 2013, MNRAS, 433, 3297
Dubois, Y., Peirani, S., Pichon, C., et al. 2016, MNRAS, 463, 3948
Duc, P.-A., Cuillandre, J.-C., Karabal, E., et al. 2015, MNRAS, 446, 120
Fabjan, D., Borgani, S., Tornatore, L., et al. 2010, MNRAS, 401, 1670
Forbes, D. A., & Remus, R.-S. 2018, MNRAS, 479, 4760
Forbes, D. A., & Thomson, R. C. 1992, MNRAS, 254, 723
Graham, A. W. 2013, in Elliptical and Disk Galaxy Structure and Modern Scaling Laws, ed. T. D. Oswalt & W. C. Keel, Vol. 6 (Dordrecht: Springer), 91
Harris, W. E., Remus, R.-S., Harris, G. L. H., & Babyk, I. V. 2020, ApJ, 905, 28
Hernquist, L., & Barnes, J. E. 1991, Natur, 354, 210
Hilz, M., Naab, T., & Ostriker, J. P. 2013, MNRAS, 429, 2924
Hilz, M., Naab, T., Ostriker, J. P., et al. 2012, MNRAS, 425, 3119
Hirschmann, M., Dolag, K., Saro, A., et al. 2014, MNRAS, 442, 2304
Hirschmann, M., Naab, T., Ostriker, J. P., et al. 2015, MNRAS, 449, 528
Huang, S., Ho, L. C., Peng, C. Y., Li, Z.-Y., & Barth, A. J. 2013, ApJ, 766, 47
Hudson, M. J., Gillis, B. R., Coupon, J., et al. 2015, MNRAS, 447, 298
Karademir, G. S., Remus, R.-S., Burkert, A., et al. 2019, MNRAS, 487, 318
Kluge, M., Neureiter, B., Riffeser, A., et al. 2020, ApJS, 247, 34
Komatsu, E., Smith, K. M., Dunkley, J., et al. 2011, ApJS, 192, 18
Kormendy, J., Fisher, D. B., Cornell, M. E., & Bender, R. 2009, ApJS, 182, 216
Kravtsov, A. V., Vikhlinin, A. A., & Meshcheryakov, A. V. 2018, AstL, 44, 8
Lagos, C. d. P., Stevens, A. R. H., Bower, R. G., et al. 2018, MNRAS, 473, 4956
Lange, R., Driver, S. P., Robotham, A. S. G., et al. 2015, MNRAS, 447, 2603
Lotz, M., Dolag, K., Remus, R.-S., & Burkert, A. 2021, MNRAS, 506, 4516
Ludlow, A. D., Schaye, J., Schaller, M., & Richings, J. 2019, MNRAS, 488, L123
Matthee, J., Schaye, J., Crain, R. A., et al. 2017, MNRAS, 465, 2381
Merritt, A., van Dokkum, P., Abraham, R., & Zhang, J. 2016, ApJ, 830, 62
Moster, B. P., Naab, T., & White, S. D. M. 2020, MNRAS, 499, 4748
Naab, T., Johansson, P. H., & Ostriker, J. P. 2009, ApJL, 699, L178
Oser, L., Naab, T., Ostriker, J. P., & Johansson, P. H. 2012, ApJ, 744, 63
Oser, L., Ostriker, J. P., Naab, T., Johansson, P. H., & Burkert, A. 2010, ApJ, 725, 2312
Pillepich, A., Nelson, D., Hernquist, L., et al. 2018, MNRAS, 475, 648
Pillepich, A., Vogelsberger, M., Deason, A., et al. 2014, MNRAS, 444, 237
Poci, A., McDermid, R. M., Zhu, L., & van de Ven, G. 2019, MNRAS, 487, 3776
Pulsoni, C., Gerhard, O., Arnaboldi, M., et al. 2021, A&A, 647, A95
Purcell, C. W., Bullock, J. S., & Zentner, A. R. 2007, ApJ, 666, 20
Qu, Y., Helly, J. C., Bower, R. G., et al. 2017, MNRAS, 464, 1659
Ragagnin, A., Dolag, K., Biffi, V., et al. 2017, A&C, 20, 52
Ragusa, R., Mirabile, M., Spavone, M., et al. 2022, FrASS, 9, 852810
Remus, R.-S., Dolag, K., Naab, T., et al. 2017, MNRAS, 464, 3742
Rodriguez-Gomez, V., Pillepich, A., Sales, L. V., et al. 2016, MNRAS, 458, 2371
Schulze, F., Remus, R.-S., Dolag, K., et al. 2020, MNRAS, 493, 3778
Schulze, F., Remus, R.-S., Dolag, K., et al. 2018, MNRAS, 480, 4636
Schweizer, F., & Seitzer, P. 1992, AJ, 104, 1039
Seigar, M. S., Graham, A. W., & Jerjen, H. 2007, MNRAS, 378, 1575
Sérsic, J. L. 1963, BAAA, 6, 41
Spavone, M., Capaccioli, M., Napolitano, N. R., et al. 2017, A&A, 603, A38
Spavone, M., Iodice, E., van de Ven, G., et al. 2020, A&A, 639, A14
Springel, V., & Hernquist, L. 2005, ApJL, 622, L9
Springel, V., White, S. D. M., Tormen, G., & Kauffmann, G. 2001, MNRAS, 328, 726
Steinborn, L. K., Dolag, K., Comerford, J. M., et al. 2016, MNRAS, 458, 1013
Steinborn, L. K., Dolag, K., Hirschmann, M., Prieto, M. A., & Remus, R.-S. 2015, MNRAS, 448, 1504
Tacchella, S., Diemer, B., Hernquist, L., et al. 2019, MNRAS, 487, 5416
Tal, T., & van Dokkum, P. G. 2011, ApJ, 731, 89
Tal, T., van Dokkum, P. G., Nelan, J., & Bezanson, R. 2009, AJ, 138, 1417
Teklu, A. F., Remus, R.-S., Dolag, K., et al. 2018, ApJL, 854, L28
Teklu, A. F., Remus, R.-S., Dolag, K., et al. 2015, ApJ, 812, 29
Teklu, A. F., Remus, R.-S., Dolag, K., & Burkert, A. 2017, MNRAS, 472, 4769
Tornatore, L., Borgani, S., Dolag, K., & Matteucci, F. 2007, MNRAS, 382, 1050
Tornatore, L., Borgani, S., Matteucci, F., Recchi, S., & Tozzi, P. 2004, MNRAS, 349, L19
Tortora, C., La Barbera, F., Napolitano, N. R., et al. 2014, MNRAS, 445, 115
Tortora, C., Posti, L., Koopmans, L. V. E., & Napolitano, N. R. 2019, MNRAS, 489, 5483
van de Sande, J., Lagos, C. D. P., Welker, C., et al. 2019, MNRAS, 484, 869
Vogelsberger, M., Marinacci, F., Torrey, P., & Puchwein, E. 2020, NatRP, 2, 42
Wiersma, R. P. C., Schaye, J., & Smith, B. D. 2009, MNRAS, 393, 99
Zheng, Z., Thilker, D. A., Heckman, T. M., et al. 2015, ApJ, 800, 120